

# Nuclear Input for Core-collapse Models

Gabriel Martínez-Pinedo<sup>a</sup>, Matthias Liebendörfer<sup>b</sup>, and  
Dieter Frekers<sup>c</sup>

<sup>a</sup>*ICREA and Institut d'Estudis Espacials de Catalunya, Universitat Autònoma de  
Barcelona, E-08193 Bellaterra, Spain*

<sup>b</sup>*Canadian Institute for Theoretical Astrophysics, Toronto, ON M5S 3H8, Canada*

<sup>c</sup>*Institut für Kernphysik, Westfälische Wilhelms-Universität Münster, D-48149  
Münster, Germany*

---

## Abstract

We review the nuclear physics input necessary for the study of the collapse of massive stars as precursor to supernova explosions. Recent theoretical advances for the calculation of the relevant weak-interaction processes and their influence in the collapse and postbounce dynamics are discussed. Future improvements are expected to come with the advent of radioactive ion-beam facilities.

---

## 1 Introduction

Stars with masses exceeding roughly  $10 M_{\odot}$  reach a moment in their evolution when their iron core provides no further source of nuclear energy generation. At this time, they collapse and, if not too massive, bounce and explode in spectacular events known as type II or Ib/c supernovae. These explosions mark the formation of a neutron star or black hole at the end of the life of the star and play a preeminent role in the nucleosynthesis and chemical evolution of the galaxy. The evolution in the core is determined by the competition of gravity, that produces the collapse of the core, and the weak interaction, that determines the rate at which electrons are captured and the rate at which neutrinos are trapped during the collapse.

The early phases, known as presupernova evolution, follow the late-stage stellar evolution until core densities just below  $10^{10} \text{ g cm}^{-3}$  and temperatures between 5 and 10 GK are reached. Stellar evolution until this time requires the consideration of an extensive nuclear network, but is simplified by the fact that neutrinos need only be treated as a sink of energy and lepton number. This is no longer valid at later stages of the collapse: as the weak in-

teraction rates increase with the increasing density, the neutrino mean free paths become shorter so that the neutrinos eventually proceed through all phases of free streaming, diffusion, and trapping. An adequate handling of the transitions between these transport regimes necessitates a detailed time- and space-dependent bookkeeping of the neutrino distributions in the core. During collapse, only the electron neutrinos,  $\nu_e$ , are important because the positron abundance, which would lead to electron antineutrino emission by capture on neutrons, is very low under electron-degenerate conditions. Later in the evolution the electron degeneracy is partially lifted and in addition to the electron flavor neutrinos also heavy neutrinos,  $\nu_\mu$ ,  $\nu_\tau$ , and their antiparticles, are usually included in numerical simulations of core collapse and postbounce evolution.

Advantageously, the temperature during the collapse and explosion are high enough that the matter composition is given by nuclear statistical equilibrium without the need of reaction networks for the strong and electromagnetic interaction. The transition from a rather complex global nuclear network, involving many neutron, proton and  $\alpha$  fusion reactions and their inverses, to a quasi-statistical equilibrium, in which reactions within mini-cycles are fast enough to bring constrained regions of the nuclear chart into equilibrium, to finally global nuclear statistical equilibrium is extensively discussed by [1].

The crucial weak processes during the collapse and postbounce evolution are [2,3,4,5,6]

$$p + e^- \rightleftharpoons n + \nu_e \tag{1}$$

$$n + e^+ \rightleftharpoons p + \bar{\nu}_e \tag{2}$$

$$(A, Z) + e^- \rightleftharpoons (A, Z - 1) + \nu_e \tag{3}$$

$$(A, Z) + e^+ \rightleftharpoons (A, Z + 1) + \bar{\nu}_e \tag{4}$$

$$\nu + N \rightleftharpoons \nu + N \tag{5}$$

$$N + N \rightleftharpoons N + N + \nu + \bar{\nu} \tag{6}$$

$$\nu + (A, Z) \rightleftharpoons \nu + (A, Z) \tag{7}$$

$$\nu + e^\pm \rightleftharpoons \nu + e^\pm \tag{8}$$

$$\nu + (A, Z) \rightleftharpoons \nu + (A, Z)^* \tag{9}$$

$$e^+ + e^- \rightleftharpoons \nu + \bar{\nu} \tag{10}$$

$$(A, Z)^* \rightleftharpoons (A, Z) + \nu + \bar{\nu} \tag{11}$$

$$\nu_e \bar{\nu}_e \rightleftharpoons \nu_{\mu,\tau} \bar{\nu}_{\mu,\tau} \tag{12}$$

Here, a nucleus is symbolized by its mass number  $A$  and charge  $Z$ ,  $N$  denotes either a neutron or a proton and  $\nu$  represents any neutrino or antineutrino. We note that, according to the generally accepted collapse picture [7], elastic scattering of neutrinos on nuclei (7) is mainly responsible for the trapping, as it determines the diffusion time scale of the outwards streaming neutrinos.

Shortly after trapping, the neutrinos are thermalized by energy downscattering, experienced mainly in inelastic scattering off electrons (8). The relevant cross sections for these processes are collected in appendix C of Ref. [2] (for an update see Ref. [6] in this volume). Reactions (1) and (3) are equally important, as they control the neutronization of the matter and, in a large portion, also the star's energy losses. Due to their strong phase space sensitivity ( $\sim E_e^5$ ), the electron capture rates increase rapidly during the collapse as the density (the electron chemical potential scales like  $\sim \rho^{1/3}$ ) and the temperature increase. In the postbounce phase, it is neutrino-nucleon scattering, Eq. (5), that provides the main opacity, and lepton capture on nucleons, eqs. (1) and (2), that are responsible for the dominant creation and absorption of electron flavor neutrinos. While reactions (4), (9) and (11) have not yet been routinely included in dynamical models, nucleon-nucleon bremsstrahlung [8,9], Eq. (6), and  $\nu_e\bar{\nu}_e$  annihilation [10,11,12], Eq. (12), have replaced the traditional electron-positron annihilation, Eq. (10), in the role of the dominant source for  $\mu$  and  $\tau$  neutrinos.

Numerical simulations of core collapse have a long history (see Ref. [7] and references therein). After the observation of the closeby supernova 1987A in the Magellanic Cloud, simulations in spherical symmetry reached a climax around 1990. At that time it was established that the neutrino transport scheme has to be performed in separate energy groups to account for the strong ( $\propto E_\nu^2$ ) energy dependence of the neutrino cross sections and it was realized that the thermalization of the neutrino distribution function by neutrino-electron scattering plays an important role in the deleptonization and core dynamics [2,13,14,15,16,17]. Most simulations relied on the flux-limited diffusion equation for the neutrinos. The accuracy of this approximation in the collapse phase was evaluated by comparison to approaches where the full Boltzmann transport equation was solved [3]. It took another decade until these more sophisticated schemes also mastered the postbounce phase in general relativistic space-time [18,4]. The narrowing technical uncertainties in spherically symmetric simulations and the accessible information about the detailed neutrino distribution functions sparked new interest to improve the nuclear and weak interaction physics ingredients. These efforts coincided with the development of large-scale shell model calculations (see Ref. [19] for a review) that allowed for a more sophisticated and accurate treatment of electron capture rates for the presupernova and collapse phases [5,20,21]. Moreover, the shell-model calculations could be validated [22] against the experimental data on GT distribution measured on charge-exchange experiments. The advent of new radioactive ion beam facilities and high resolution experimental techniques based on the ( $t, {}^3\text{He}$ ) [23,24] and ( $d, {}^2\text{He}$ ) [25,26] charge-exchange reactions will contribute to an improved treatment of the electron capture rates used in simulations.

No spherically symmetric simulation of core collapse and postbounce evolu-

tion with accurate neutrino transport produced an explosion [27,28,29,30,31], neither by the prompt bounce-shock mechanism, nor by the delayed neutrino-heating mechanism. Despite the mentioned progress in simulation technique and input physics, it became very evident that the complicated dynamics of the delayed supernova explosion can no longer be expected to be captured in spherically symmetric simulations. It has been shown that the heating region is unstable to convective overturn which significantly improves the efficiency of the neutrino heating behind the stalled bounce-shock [32,33,34]. However, later investigations with two-dimensional hydrodynamics and more accurate (particularly energy-dependent) neutrino transport still failed to reproduce vigorous supernova explosions [35,36]. Furthermore, suggestions that an enhanced neutrino luminosity due to neutron finger convection in the protoneutron star [17] could increase the heating behind the shock are also not confirmed by recent analytical analysis [37]. Hence, more ingredients to a realistic supernova model must be missing or inadequately be accounted for. There are however indications, that an additional twist might suffice to at least produce an explosion, like for example a very asymmetric deformation of the standing accretion shock [38,39] or effects from magnetic fields [40,41,42,43].

In this review we will discuss nuclear physics ingredients to which core collapse supernovae are sensitive. The manuscript is organized as follows: first we discuss the role of weak interactions in the presupernova evolution. Then we comment on the main hydrodynamical features of core collapse based on a realistic nuclear equation of state. We will see that the dynamics is governed by entropy changes and deleptonization, which we then investigate in detail with respect to traditional and new nuclear physics ingredients. Finally, we discuss the influence of the recently improved collapse physics on the post-bounce evolution.

## 2 Presupernova evolution

The main weak interaction processes during the final evolution of a massive star are electron capture and beta decays. Its determination requires the calculation of Fermi and Gamow-Teller (GT) transitions. While the treatment of Fermi transitions (important only for beta decays) is straightforward, a correct description of the GT transitions is a difficult problem in nuclear structure. In the astrophysical environment nuclei are fully ionized, so one has continuum electron capture from the degenerate electron plasma. The energies of the electrons are high enough to induce transitions to the Gamow-Teller resonance. Shortly after the discovery of these collective excitation Bethe *et al.* [44] recognized its importance for stellar electron capture. This process is mainly sensitive to the location, fragmentation and total strength of the Gamow-Teller resonance. The presence of a degenerate electron gas blocks the phase

space for the produced electron in beta decay. Then, the decay rate of a given nuclear state is greatly reduced or even completely blocked at high densities. However, due to the finite temperature, excited states in the decaying nucleus can be thermally populated. Some of these states are connected by large GT transitions to low-lying states in the daughter nucleus, which with increased phase space can significantly contribute to the stellar beta decay rates. The importance of these states in the parent nucleus for the beta decay was first recognized by Fuller, Fowler and Newman (FFN) [45,46,47,48], who coined the term “backresonances” (see figure 1).

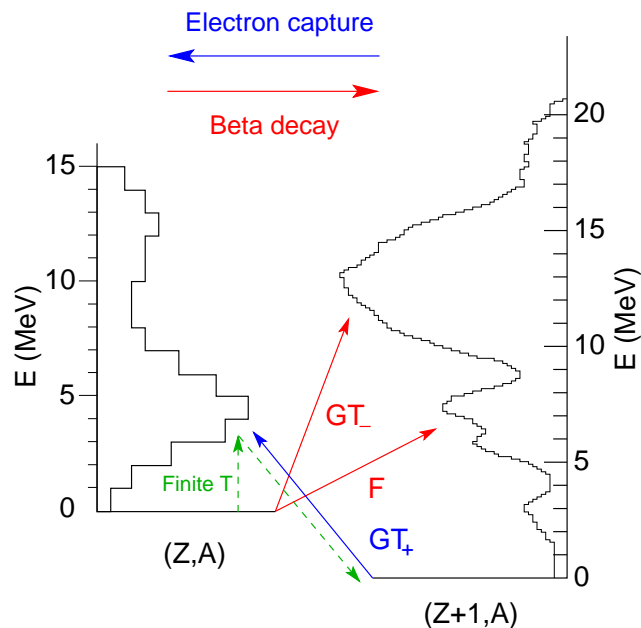


Fig. 1. The figure shows schematically the electron-capture and beta-decay processes in the stellar environment. Electron capture proceeds by Gamow-Teller transitions to the  $GT_+$  resonance. In the case of beta decay both the Fermi and Gamow-Teller resonances are typically outside the  $Q_\beta$  window and hence not populated in the beta decay. Due to the finite temperature in the stellar environment, excited states in the decaying nucleus can be thermally populated. Some of these states have large GT transitions to low lying states in the daughter nucleus. These states in the decaying nucleus are called “backresonances”

Over the years many calculations of weak interaction rates for astrophysical applications have become available [49,50,51,52,53,54,55]. For approximately 15 years, though, the standard in the field were the tabulations of Fuller, Fowler and Newman [45,46,47,48]. These authors calculated rates for electron capture, positron capture, beta decay and positron emission plus the associated neutrino losses for all the astrophysical relevant nuclei ranging in mass number from 21 to 60. Their calculations were based upon an examination of all available experimental information in the mid 1980s for individual transitions between ground states and low-lying excited states in the nuclei of interest. Recognizing that this only saturated a small part of the Gamow-Teller distribution, they added the collective strength via a single-state represen-

tation whose position and strength was parametrized using an independent particle model.

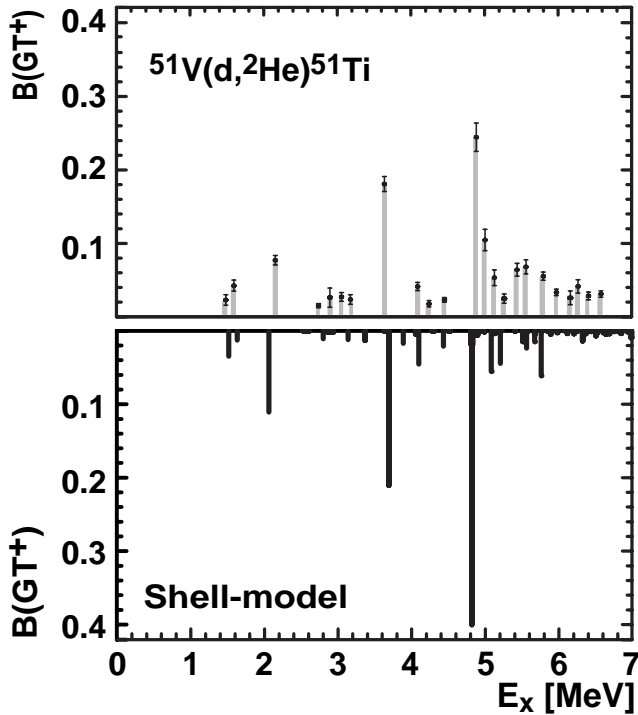


Fig. 2. Comparison of the shell-model  $GT_+$  distribution (lower panel) for  $^{51}\text{V}$  with the high resolution  $(d, ^2\text{He})$  data [56]. The shell-model distribution includes a quenching factor of  $(0.74)^2$ .

Recent experimental data on  $GT$  distributions in iron group nuclei [57,58,59,60,61,62,63,64], measured in charge exchange reactions [65,66], show that the  $GT$  strength is strongly quenched (reduced), compared with the independent-particle-model value, and fragmented over many states in the daughter nucleus. Both effects are caused by the residual interaction among the valence nucleons. An accurate description of these correlations is essential for a reliable evaluation of the stellar weak-interaction rates due to the large dependence of the available phase-space on the electron energy, particularly for the stellar electron-capture rates [45,20]. The shell-model is the only known tool to reliably describe  $GT$  distributions in nuclei [67]. Indeed, Ref. [22] demonstrated that the shell-model reproduces very well all measured  $GT_+$  distributions (in this direction a proton is converted to a neutron, as in electron capture) for nuclei in the iron mass range and gives a very reasonable account of the experimentally known  $GT_-$  distributions (in this direction a neutron is converted to a proton, as in  $\beta$  decay). However, the limited experimental resolution ( $\sim 1$  MeV) achieved by the pioneering  $(n, p)$ -type charge-exchange experiments did not allow for a detailed determination of the fragmentation of the  $GT$  strength in individual states. Very recently, high-resolution  $GT_+$  distributions measured at KVI, via the  $(d, ^2\text{He})$  reaction, have become available for two iron group nuclei,  $^{51}\text{V}$  [56] and  $^{58}\text{Ni}$  [68]. The experimental data for  $^{51}\text{V}$  are compared in figure 2 with a

shell-model calculation using the KB3G interaction [69].

Several years ago, it was pointed out that the interacting shell model is the method of choice for the calculation of stellar weak-interaction rates [55,70,71,72,73]. Following the work of Ref. [67], shell-model rates for all the relevant weak processes for *sd*-shell nuclei ( $A = 17\text{--}39$ ) were calculated in Ref. [74]. This work was then extended to heavier nuclei ( $A = 45\text{--}65$ ) based on shell-model calculations in the complete *pf*-shell [20,75]. Following the spirit of FFN, the shell model results have been replaced by experimental data (energy positions, transition strengths) wherever available.

Ref. [20] compares the shell-model based rates with the ones computed by FFN. The shell-model rates are nearly always smaller than the FFN ones at the relevant temperatures and densities. The differences are caused by a reduction of the Gamow-Teller strength (quenching) compared to the independent-particle-model value and a systematic misplacement of the Gamow-Teller centroid (mean energy value of the Gamow-Teller distribution) in nuclei depending on the pairing structure. In some cases, experimental data that were not available to Fuller, Fowler and Newman, but could be used now, led to significant changes.

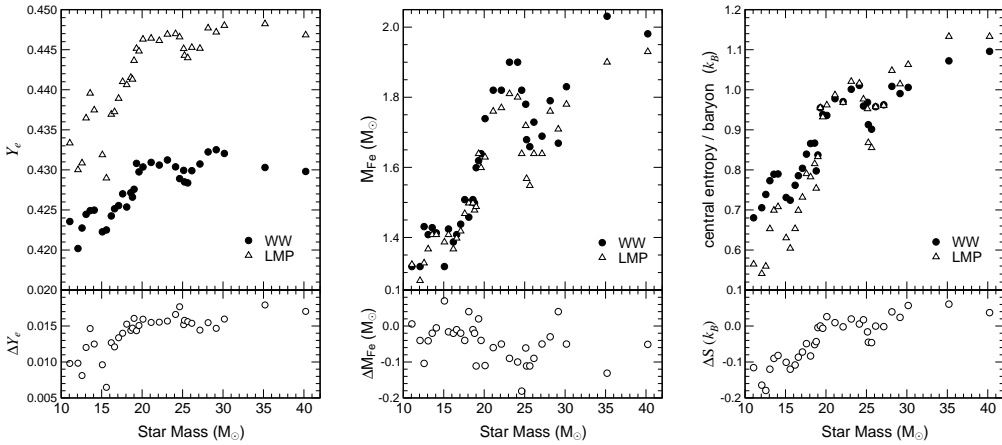


Fig. 3. Comparison of the center values of  $Y_e$  (left), the iron core sizes (middle) and the central entropy (right) for 11–40  $M_{\odot}$  stars between the WW models and the ones using the shell model weak interaction rates (LMP) [76]. The lower parts define the changes in the 3 quantities between the LMP and WW models.

The influence of the shell-model rates in the late-stage evolution of massive stars has been investigated in Ref. [76,77] repeating the calculations of Ref. [78], keeping the stellar physics as close to the original studies as possible. The new calculations incorporated the shell-model based weak-interaction rates for nuclei with mass numbers  $A = 45\text{--}65$ , supplemented by the *sd*-shell nuclei rates from Ref. [74]. The earlier calculations of Woosley and Weaver (WW) used the FFN rates for electron capture and an older set of beta decay rates [51,52]. Figure 3 illustrates the consequences of the shell model weak

interaction rates for presupernova models in terms of the three decisive quantities: the central electron-to-baryon ratio  $Y_e$ , the entropy, and the iron core mass. The central values of  $Y_e$  at the onset of core collapse increased by 0.01–0.015 for the new rates. This is a significant effect. For example, a change from  $Y_e = 0.43$  in the WW model for a  $20 M_\odot$  star to  $Y_e = 0.445$  in the new models increases the respective Chandrasekhar mass by about  $0.075 M_\odot$ . We note that the new models also result in lower core entropies for stars with  $M \leq 20 M_\odot$ , while for  $M \geq 20 M_\odot$ , the new models actually have a slightly larger entropy. The iron core masses are generally smaller in the new models where the effect is larger for more massive stars ( $M \geq 20 M_\odot$ ), while for the most common supernovae ( $M \leq 20 M_\odot$ ) the reduction is by about  $0.05 M_\odot$ . [We define the iron core as the mass interior to the point where the composition becomes at least 50% of iron group elements ( $A \geq 48$ )]. This reduction of the iron core mass appears to be counterintuitive at first glance with respect to the slower electron capture rates in the new models. It is, however, related to changes in the entropy profile during silicon shell burning which reduces the growth of the iron core just prior to collapse [76].

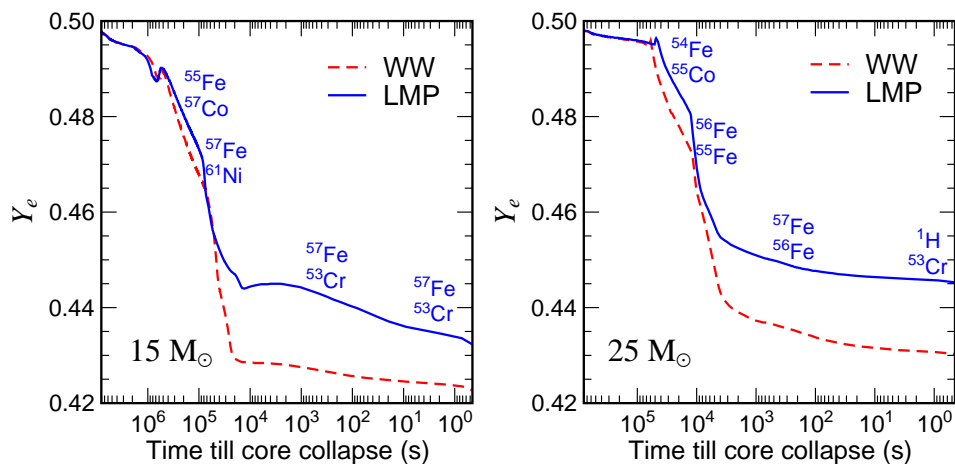


Fig. 4. Evolution of the  $Y_e$  value in the center of a  $15 M_\odot$  star (left panel) and a  $25 M_\odot$  star (right panel) as a function of time until bounce. The dashed line shows the evolution in the Woosley and Weaver models (WW) [78], while the solid line shows the results using the shell-model based weak-interaction rates of Langanke and Martínez-Pinedo (LMP). The most important nuclei in the determination of the electron-capture rate for the calculations adopting the shell model rates are indicated at different times.

To understand the origin of these differences it is illustrative to investigate the role of the weak-interaction rates in greater detail. The evolution of  $Y_e$  during the presupernova phase is plotted in figure 4. Weak processes become particularly important in reducing  $Y_e$  below 0.5 after oxygen depletion ( $\sim 10^7$  s and  $10^6$  s before core collapse for the  $15 M_\odot$  and  $25 M_\odot$  stars, respectively) and  $Y_e$  begins a decline which becomes precipitous during silicon burning. Initially electron capture occurs much more rapidly than beta decay. As the shell model rates are generally smaller than the FFN electron capture rates, the



initial reduction of  $Y_e$  is smaller in the new models; the temperature in these models is correspondingly larger as less energy is radiated away by neutrino emission.

An important feature of the new models is shown in the left panel of figure 4. For times between  $10^4$  and  $10^3$  s before core collapse,  $Y_e$  increases due to the fact that beta decay becomes temporarily competitive with electron capture after silicon depletion in the core and during silicon shell burning. This had been foreseen in Ref. [79]. The presence of an important beta decay contribution has two effects. Obviously it counteracts the reduction of  $Y_e$  in the core, but equally important, beta decays are an additional neutrino source and thus they add to the cooling of the core and a reduction in entropy. This cooling can be quite efficient as often the average neutrino energy in the involved beta decays is larger than for the competing electron captures. As a consequence the new models have significantly lower core temperatures than the WW models after silicon burning. At later stages of the collapse, beta decay becomes unimportant again as an increased electron chemical potential drastically reduces the phase space.

We note that the shell model weak interaction rates predict the presupernova evolution to proceed along a temperature-density- $Y_e$  trajectory where the weak processes are dominated by nuclei rather close to stability. Thus it will be possible, after next generation radioactive ion-beam facilities become operational, to further constrain the shell model calculations by measuring relevant GT distributions for unstable nuclei by charge-exchange reaction, where we emphasize that the  $GT_+$  distribution is also crucial for stellar  $\beta$ -decays [71]. Figure 4 identifies those nuclei which dominate (defined by the product of abundance times rate) the electron capture during various stages of the final evolution of  $15 M_\odot$  and  $25 M_\odot$  stars. An exhaustive list of the most important nuclei for both electron capture and beta decay during the final stages of stellar evolution for stars of different masses is given in Ref. [77]

In total, the weak interaction processes shift the matter composition to smaller  $Y_e$  values (see Fig. 4) and hence more neutron-rich nuclei, subsequently affecting the nucleosynthesis. Its importance for the elemental abundance distribution, however, strongly depends on the location of the mass cut in the supernova explosion. It is currently assumed that the remnant will have a larger baryonic mass than the iron core, but smaller than the mass enclosed by the oxygen shell [80]. As the reduction of  $Y_e$  occurs mainly during silicon burning, it is essential to determine how much of this material will be ejected. Moreover, as show in refs. [81,82,83], weak interactions determine the composition of the innermost supernova ejecta. Another important issue is the possible long-term mixing of material during the explosion [84]. Changes of the elemental abundances due to the improved weak-interaction rates are rather small because the differences with respect to FFN occur in regions of

the star which are probably not ejected.

### 3 Core-Collapse and Bounce

#### 3.1 Hydrodynamics

At the onset of collapse of the progenitor model, the core dynamics becomes relevant. The dynamics of core collapse is an interesting example where numerical simulation stimulated the analytical understanding. Early spherically symmetric simulations (at that time adiabatic or based on leakage schemes) [85,86,87,88] suggested the separation of the collapsing material into an inner and an outer core. The inner core fails only marginally to be pressure supported and the sound speed stays faster than the fluid velocity at all times. Under these conditions, the velocity develops to a linear function of the radius. However, because the matter density and sound speed decrease with increasing radius, there is a sonic point where the infall velocity exceeds the sound speed so that information about the collapsing inner core ceases to reach the outer layers. The outer layers therefore rather assume a free fall velocity profile in the rarefaction of the homologously collapsing inner core. In the following we review different factors that determine the size of the inner core and try to draw the connection to the initial energy imparted to the bounce-shock.

Figure 5 shows typical scales for energy densities as a function of the rest mass density,  $\rho$ . The data has been taken from model G15 [31] which has been evolved with general relativistic Boltzmann neutrino transport. A time slice at bounce is shown. The order of magnitude of the energy density is given by the gravitational binding energy of mass shells (thick solid line). It is balanced by the kinetic energy (dash-dotted line) and the internal energy. The latter determines the fluid pressure, composed from the electron pressure (thin solid line), baryonic pressure (dotted line) and neutrino pressure (dashed line). The dominant pressure of the relativistic electrons scales with  $\rho^{4/3}$  over a large density range (in Fig. 5 actually somewhat shallower due to the radial variations in the electron fraction,  $Y_e$ ).

The essentially polytropic behavior of the equation of state allows an analytic investigation [90,91] of collapse. It shows that the mass of the inner core,  $M_{\text{ic}}$ , is well approximated by

$$M_{\text{ic}} \simeq (\kappa/\kappa_0)^{3/2} M_0, \quad (13)$$

where  $M$  refers to the core mass and  $\kappa$  to the coefficient in the polytropic equation of state  $p = \kappa\rho^\gamma$  with  $\gamma = 4/3$ . Values with index 0 belong to the

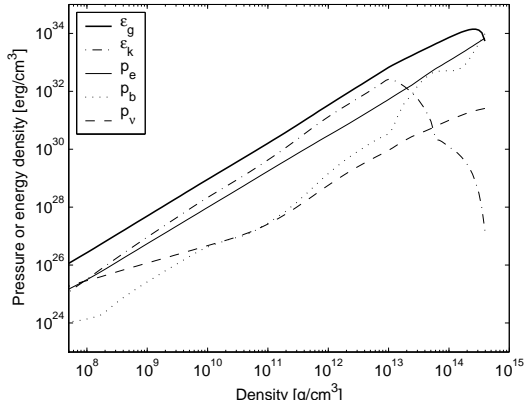


Fig. 5. Energy densities as functions of rest mass density at bounce in model G15 [31]. Shown are the gravitational energy density,  $\varepsilon_g$ , and the kinetic energy density,  $\varepsilon_k$ . The total pressure splits into the electron pressure,  $p_e$ , the baryonic pressure,  $p_b$ , and the neutrino pressure,  $p_\nu$ . The latter has been determined by taking the second angular momentum of the radiation intensity. Note that the dynamics barely depends on the neutrino pressure because of the dominant electron pressure at high density and the negligible coupling between neutrinos and matter at low density [89].

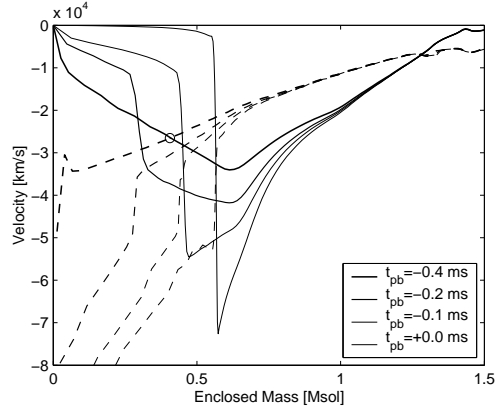


Fig. 6. Velocity profiles at bounce (solid lines). The time after maximum central density,  $t_{pb}$ , is negative before bounce. The maximum infall velocity at 0.4 ms before bounce marks the edge of the inner core at that time. A circle is drawn at the sonic point. The later profiles demonstrate how a pressure wave is launched at the center which runs through the inner core to turn into a shock front close to its edge. The dashed lines represent the sound speed as given by the Lattimer-Swesty equation of state.

marginally stable stage immediately before collapse. With the coefficient for the degenerate ultra-relativistic electron gas [92],

$$\kappa = \frac{\hbar c}{4} (3\pi^2)^{1/3} \left( \frac{Y_e}{m_B} \right)^{4/3}, \quad (14)$$

one readily reproduces the conclusion that the mass of the inner core evolves proportionally to  $Y_e^2$ . The evolution of the electron fraction is therefore the most significant ingredient to determine the mass of the inner core at bounce. Note that the pressure of trapped neutrinos does not reach the level of the electron pressure because their chemical potential is lower in accordance to the difference between the neutron and proton chemical potentials (cf. Fig. 7).

The analytical approach becomes more complex for a general adiabatic index  $\gamma \leq 4/3$ . Nevertheless, it is possible to express the selfsimilar solution in terms of a time-independent density profile  $D(X)$ , where  $X$  is a self-similarity variable. The inner core mass then scales with time,  $t$ , as [91]

$$M_{ic} = \kappa^{3/2} G^{(1-3\gamma)/2} (t_{\text{bounce}} - t)^{4-3\gamma} M(X) \quad (15)$$

$$M(X) = 4\pi \int_0^X dx x^2 D(x).$$

$G$  is the gravitational constant,  $M(X)$  is the mass enclosed inside the similarity variable  $X$ , and  $t_{\text{bounce}}$  is the time at bounce. The analysis demonstrates that there is a dependence of the hydrodynamics of core collapse on the adiabatic index of the equation of state at subnuclear densities. Due to the dominance of the electron pressure, however, deviations from  $\gamma = 4/3$  cannot be large.

The analytical analysis is only valid in the nonrelativistic limit. General relativistic numerical simulations lead to a significantly smaller mass of the inner core [93]. Equation (15) predicts that the mass of the inner core decreases with time if the adiabatic index falls below the critical value for a stable core in Newtonian gravitation, i.e.  $\gamma = 4/3$ . In general relativity, the effective gravitational potential is deeper and the critical adiabatic index for stability is larger [94]. One may therefore argue that in the general relativistic case even the  $\gamma = 4/3$  from the ultra-relativistic electron gas falls below the critical adiabatic index. Hence, the inner core shrinks during collapse as suggested by Eq. (15). A rigorous argument, however, would have to rely on an analytical analysis of core collapse based on a general relativistic similarity variable [95]. Recent numerical simulations of core collapse specify a reduction of about 20% in the inner core mass due to general relativistic effects [29,18,96]. The size of the inner core is most important for the energetics of the core-bounce:

The baryonic pressure displayed in Fig. 5 (dotted line) increases steeply at high density. Shortly above  $10^{13}$  g/cm<sup>3</sup> the thermal pressure component is exceeded by the neutron degeneracy pressure. The plateau across the phase transition from isolated nuclei to bulk nuclear matter at  $10^{14}$  g/cm<sup>3</sup> is caused by the attractive nuclear forces. The phase transition with its many possible geometrical structures and statistical fragmentation is very interesting from a nuclear physics point of view [97,98,99,100]. However, a significant impact of the microscopic phenomena in this regime on the collapse and/or supernova dynamics remains to be demonstrated. At and above saturation density, repulsive nuclear forces dominate the stiffness of the equation of state. When the center of the collapsing core reaches these densities, collapse is halted by an outgoing pressure wave. This pressure wave travels through the inner core, where infall velocities are subsonic, and turns into a shock wave close to its edge. The matter in the inner core experiences a rather adiabatic pressure wave and remains at a low entropy  $\sim 1.4$  kB per baryon. The shock wave in the outer core, however, heats matter to entropies larger than  $\sim 6$  kB per baryon so that heavy nuclei are dissociated. If the bounce-shock were to dynamically propagate through the core to expel outer layers in a prompt explosion, it would have to provide the energy to dissociate the material between the edges of the inner core and the iron core at a rate of  $1.5 \times 10^{51}$  erg per  $0.1 M_{\odot}$  of

dissociated material (the shock additionally suffers from unavoidable neutrino losses).

The size of the inner core does not only set the mass that will be dissociated in the postbounce evolution, additionally it determines the initial energy of the bounce-shock. The rebound of a larger mass in the gravitational potential implies a larger initial energy imparted to the outgoing shock wave. This initial shock energy has been found to depend sensitively on the stiffness of the equation of state around nuclear densities [94,101,102,15,103,104,39]. Unfortunately, most studies used the explosion energy of prompt hydrodynamic explosions to measure this effect. Their results are difficult to compare because the final explosion energy depends on the physics applied to propagate the initial shock through the iron core. Some apparent contradictions in the conclusions of above-cited references suggest a few retrospective comments:

The homologous core stays very large in adiabatic calculations when electron captures are neglected. Hence, energetic prompt explosions are obtained. The initial shock energy increases with a decrease of the adiabatic index in a polytropic equation of state [94]. A similar effect was found in a recent adiabatic comparison between two realistic equations of state with different incompressibilities at saturation density [104]. The period of the lowest oscillation mode of the inner core in the regime of the stiffened equation of state depends strongly on the difference of its mass from the maximum stable mass. If the mass of the inner core is much smaller than the maximum stable mass, the oscillation period is very small with respect to the sound crossing time in the outer part of the inner core. Infalling material piles up around a “hard” center until the outgoing compression wave reaches the edge of the inner core, where it turns into a relatively weak shock (see Fig. 6). If the maximum stable mass is close to the inner core mass, the oscillation period is larger and the oscillation is more efficiently excited. A larger mass bounces on a “soft” core and a more energetic shock is launched at its edge. As soon as electron captures during collapse are included, e.g. by a simple leakage scheme, the mass of the inner core shrinks and prompt explosions are more difficult to obtain. Only extremely soft equations of state lead to explosions in that case [101]. But sufficiently soft equations of state, producing a maximum stable mass close to the mass of the inner core, are not compatible with the significantly larger observed neutron star masses, unless a very extended phase transition provides softness at nuclear densities in combination with a stiff adiabatic index in the far supranuclear regime [102]. Later investigations of the effect of the equation of state at bounce were consistent with the described trend, but ceased to produce energetic prompt explosions due to improvements in the neutrino transport, especially after the inclusion of neutrino electron scattering [13,14,15]. Few years later, the BCK equation of state [105] was replaced by the Lattimer-Swesty equation of state [89] in “standard” simulations of core collapse. Its maximum mass for the hot protoneutron star is around  $2.4 M_{\odot}$ , much larger

than the mass of the inner core  $\sim 0.5 M_{\odot}$ . The consequence is a very low initial shock energy of  $1.9 \times 10^{51}$  erg (measured in simulation G15 [31] according to the definition used in Ref. [15]) instead of the  $5\text{--}10 \times 10^{51}$  erg obtained in previous studies with the BCK equation of state [15]. The dynamical shock stalls already at 3 ms after bounce. The ensuing expansion of the accretion front does not depend on the exhausted shock energy anymore. As we will briefly discuss in section 4, the expansion is determined by the accretion rate in the gravitational potential and the deleptonization rate of the accumulated matter. This explains why a comparison of different choices of incompressibilities at saturation density in Ref. [103] showed no discernible consequences for the shock propagation on a time scale of 50 ms. The study did not resolve the few milliseconds after bounce where transient effects of the compressibility variations may manifest in the energy of the short-lived bounce-shock. An update on the comparison of three different equations of state on the longer time scale of postbounce simulations with accurate neutrino transport is given in Ref. [39].

In summary, the crucial element in core collapse calculations is the determination of the mass of the inner core because it determines the point of shock formation at bounce and the initial energy that is imparted to the shock. The following paragraphs focus on the weak interactions which directly or indirectly determine the core mass through the evolution of electron fraction and entropy.

### 3.2 Deleptonization

The deleptonization and entropy changes during collapse are determined by the interplay between three different physical processes: (i) the transition of protons to neutrons by electron capture and neutrino emission (for example by reactions (1) or (3)), (ii) isoenergetic neutrino scattering (e.g. by reactions (5) or (7)), and (iii) neutrino thermalization (e.g. by reactions (8) or (9)). Each of these processes is rather straightforward to describe in a gas of free nucleons. In reality, however, the by far most abundant nuclear species in the cold collapsing matter are neutron-rich heavy nuclei (see Fig. 8). While the described weak interactions basically stay the same, they rather involve nucleons bound in nuclei than free ones. This leads to the interesting expectation that the nuclear structure is probed in many nuclei that are difficult or impossible to explore under terrestrial conditions. In the following we first describe the principle importance of each of above processes for the deleptonization of the core before we get to their detailed quantitative description and dependence on nuclear structure in section 3.3.

As the density,  $\rho$ , increases, the electron chemical potential increases with

$\mu_e \propto \rho^{1/3}$  [7], see also Fig. 7 (thin solid line). The electrons fill higher energy levels and electron captures on free or bound protons become more and more likely. As long as the density is lower than  $5 \times 10^{10}$  g/cm<sup>3</sup>, the neutrinos escape freely and the deleptonization rate is determined by the electron capture rate. Figure 9 compares the electron capture reaction rates on free protons with the electron capture reaction rates on nuclei. The former is by an order of magnitude larger than the latter. But the nuclei are by orders of magnitude more abundant targets. It is difficult to decide from first principles whether electron captures on free protons or nuclei would dominate in core collapse (see for example [44,106,107]): Because the free proton fraction is very sensitive to small variations in the  $Y_e$  value, it can be huge if the  $Y_e$  value is somewhat larger than a reference value or it can be negligible if the  $Y_e$  value is somewhat smaller than a reference value. This had interesting consequences in core collapse simulations. As described above, progenitor models for different main sequence masses or with different sophistication of the included weak interaction physics may run into collapse with quite different electron fraction profiles. Collapse simulations with Boltzmann neutrino transport, however, showed that most of the initial variations in the inner core structure converged to the same trajectories during core collapse, leading to very similar positions of shock formation and nearly identical neutrino bursts [108,109]. These simulations used the standard treatment of electron captures [2] that inhibited the dominant electron capture on nuclei as soon as nuclei exceeded neutron number  $N = 40$ . This leads to a more shallow deleptonization slope at a density  $\sim 2 \times 10^{10}$  g/cm<sup>3</sup> as illustrated in the left panel of Fig. 10. But the deleptonization is not slowed down for long because a high electron fraction at increasing density (where nuclei become more neutron rich) implies a steeply rising free proton fraction until the deleptonization resumes on a similarly effective time scale by captures on free protons. The  $Y_e$  value at which this happens is determined by the intrinsic properties of the nuclei at a given density and temperature and therefore independent from the initial electron fraction or proton abundance. Hence, the deleptonization of different models converges toward a “norm” electron fraction trajectory. A convergence of this kind will always take place when the product of electron capture reaction rate and target abundance dominates for a nucleus whose abundance strongly depends on the electron fraction.

This appears somewhat contradictory to results of earlier extensive studies of the effect of the free proton fraction on core collapse. Significant differences in the deleptonization and inner core size at bounce have been reported [14]. This result becomes understandable if one considers that the investigation has not been performed with different *initial* free proton mass fractions. Instead, different free proton mass fractions have been set by variations of the asymmetry energy in the equation of state. A smaller asymmetry energy lowers the electron fraction at which the free proton fraction becomes significant enough to perform electron captures effectively on the infall time scale. It therefore

leads to a lower “norm” trajectory for the electron fraction and to a smaller inner core at bounce. However, if the asymmetry energy is varied together with the surface energy to reproduce experimental constraints, the configuration of the nuclei is less significantly altered and similar “norm” trajectories are produced with negligible consequences for core bounce [103].

We therefore conclude that the tight feedback between electron fractions and free proton abundances defines a limiting “norm” trajectory for the deleptonization during infall. It is determined by the mass formula of nuclei according to its implementation in the equation of state. The deleptonization up to neutrino trapping can occur faster than “norm” by the availability of additional channels for electron capture, but hardly slower. The free proton mass fraction is not a relevant independent input quantity of the progenitor structure, it evolves rather symptomatically: in models that proceed along the “norm” trajectory, it is higher; in models that deleptonize faster, it is smaller. For example the most recent simulations with sophisticated nuclear input physics predict a deleptonization that is faster than the “norm” because captures on nuclei provide the most relevant electron capture channel throughout core collapse [21,96]. As we will discuss in more detail in section 3.3, the entropy also becomes slightly smaller. Both effects contribute to reduce the proton abundances when treated consistently with the hydrodynamical evolution so that electron capture on free protons becomes an almost inactive channel.

The large electron capture rates at densities higher than  $5 \times 10^{12}$  g/cm<sup>3</sup> are not relevant anymore because the neutrino scattering opacities get so large that the time scale for neutrinos to leave the star becomes larger than the production time scale. The neutrino phase space fills up and further electron captures are blocked for neutrino emission below the neutrino Fermi energy. In this regime the state of matter is best described by the density, entropy, and lepton fraction,  $Y_\ell$ . The lepton fraction becomes the independent variable that slowly changes on a diffusion time scale while the electron fraction,  $Y_e$ , almost immediately represents the local equilibrium state between the fluid and the trapped neutrino radiation field. The equilibrium is established by neutrino-electron scattering. Due to the small electron mass, the energy transfer between neutrino and the relativistic electrons is always inelastic and efficient while the much more frequent scattering between the neutrinos and the more massive nucleons and nuclei only allows for momentum transfer—at least, of course, if we neglect for a moment the possibility of intrinsic excitations of nuclei in neutrino scattering events (see section 3.4 for a discussion of that aspect).

Crucial for the total deleptonization during core collapse is the physics in the density range  $5 \times 10^{10} - 5 \times 10^{12}$  g/cm<sup>3</sup> inbetween the two extremes, free escape and trapping. Figure 7 visualizes the interplay between neutrino production,



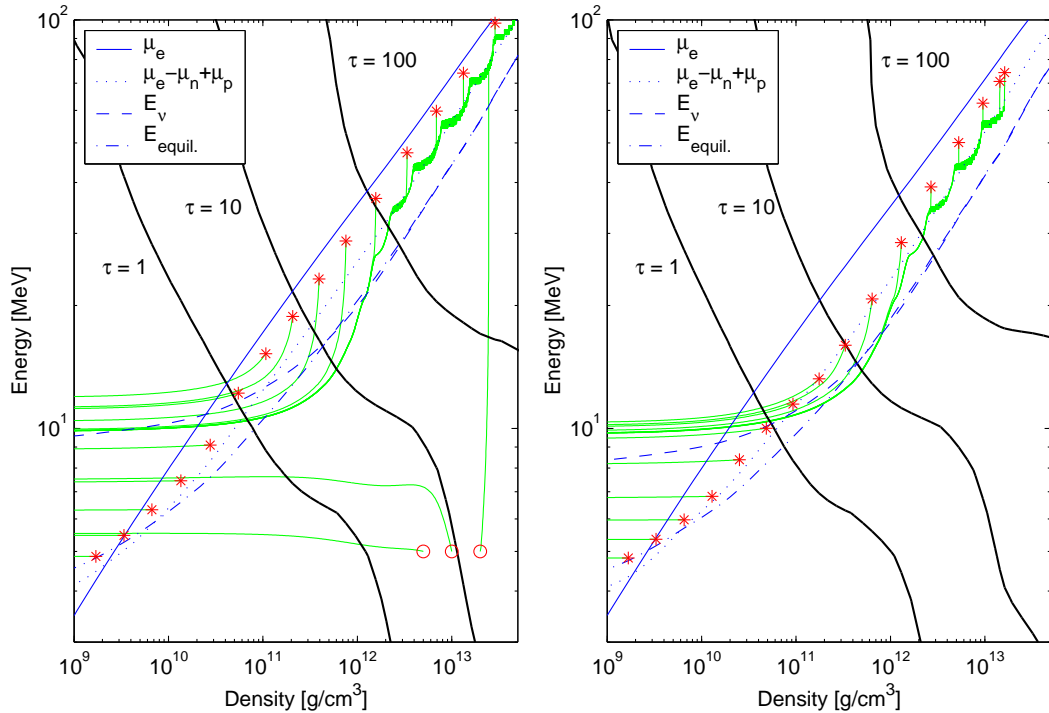


Fig. 7. Shown are the electron chemical potential,  $\mu_e$  (straight solid line), and its distance to the difference between the nucleon chemical potentials,  $\mu_e - \mu_n + \mu_p$  (dotted line). This quantity corresponds to the electron neutrino chemical potential where the neutrinos are in equilibrium with matter (recognizable in the figure as the domain where the mean neutrino energy,  $E_\nu$ , is equal to the equilibrium energy,  $E_{\text{equil}}$ ). The asterisks represent the average energy of neutrinos produced by electron capture. The neutrinos escape in a two-dimensional diffusion process in energy and space. Thick solid lines connect locations of optical depths  $\tau = 1$ ,  $\tau = 10$ , and  $\tau = 100$ . For each emitted average energy, a thin solid line indicates the trajectory of fastest escape as a function of neutrino energy and density. At subnuclear densities (e.g. circle at  $\rho = 5 \times 10^{12} \text{ g/cm}^3$ ), low energy neutrinos start to escape and to free phase space for the downscattering of higher energy neutrinos around  $\rho = 10^{11} - 10^{12} \text{ g/cm}^3$ . In this region, the figure illustrates the nontrivial interplay between neutrino emission, thermalization, and diffusion. The left panel corresponds to a time slice at bounce in model G15 [31] with conventional input physics. The right panel corresponds to a simple test calculation where, in the spirit of Ref. [110], the  $f_{5/2}$  orbit in the Bruenn scheme was unblocked to illustrate the discussion of the improved electron capture rates in section 3.3.

neutrino thermalization, and neutrino diffusion in a snapshot at bounce in model G15 [31]. Figure 7 is built around the electron chemical potential,  $\mu_e$  (thin solid line), which sets the energy scale for reactions with the degenerate electrons. Also shown is the quantity  $\mu_e - \mu_n + \mu_p$  (dotted line) where  $\mu_n - \mu_p$  is the difference between the neutron and proton chemical potentials. The quantity represents the neutrino chemical potential in regions where the neutrinos are in equilibrium with the fluid. Thick solid lines running from the upper left corner to the lower right indicate the optical depth,  $\tau$ , as a

function of density and neutrino energy. Contour lines for  $\tau = 1$  (in average one scattering before escape),  $\tau = 10$  (in average 10 scatterings before escape, etc.), and  $\tau = 100$  are shown. The contour lines approximately run along  $E^2 \rho^{2/3} = \text{const.}$  because of the increase of the scattering cross sections proportional to the squared neutrino energy [7]. The asterisks represent the average energy of emitted neutrinos by electron capture on free protons and on nuclei. For each asterisk in the graph, the trajectory of the most probable escape in the two-dimensional space of neutrino energy and matter density has been calculated and drawn with a thin solid line. Note that the trajectories only connect the most probable of all possible displacements of test neutrinos in the density-energy space. They cannot represent a rate of actual displacements. The trajectories immediately confirm that neutrinos on the left hand side of the  $\tau = 1$  line escape without further energy change while the neutrinos on the right hand side of the  $\tau = 100$  line tend to scatter to the neutrino Fermi energy on a much smaller time scale than for the diffusion in space. The holes they leave in the equilibrium distribution will immediately be refilled by new neutrino emissions or scatterings. Note also the trajectory from the additional 5 MeV test particle at  $2 \times 10^{13}$  g/cm<sup>3</sup>, which can only scatter to the Fermi surface because the neutrinos are degenerate (The small steps in the Fermi energy are of numerical nature and due to the finite resolution of the energy phase space in the multi-group neutrino treatment). The other two 5 MeV test particles at  $5 \times 10^{12}$  and  $10^{13}$  g/cm<sup>3</sup> demonstrate that at these densities very low energy neutrinos start to escape due to the relatively low scattering cross sections at these energies [51]. This frees phase space that is replenished from high energy neutrinos that are now able to down-scatter as indicated by the trajectories in the interesting density range between  $5 \times 10^{10}$  and  $5 \times 10^{12}$  g/cm<sup>3</sup>. High energy neutrinos emitted at  $10^{12}$  g/cm<sup>3</sup> finally escape with a lower energy than neutrinos emitted at a lower energy at  $10^{11}$  g/cm<sup>3</sup>. Hence, the most significant deleptonization relies on a two-dimensional diffusion process in the space spanned by neutrino energy and matter density and takes place during the transition from the density where neutrinos stream freely to the density where they are trapped.

The physics of the core collapse does not depend on the evolution of the electron fraction alone. Also the entropy plays an important role. In general the entropy is low during the collapse as most of the energy is rather stored in internal excitation energy of the nuclei than in thermal energy of the gas due to the large partition functions for nuclei [44]. However, the entropy is changed by weak interactions in the core and has important consequences for the evolution (e.g., an increase in entropy will increase the number of protons available for electron capture). The entropy change  $\Delta s$  for a deleptonization  $\Delta Y_e$  is given in Ref. [2] and references therein,

$$T\Delta s = -\Delta Y_e (\mu_e - \mu_n + \mu_p) + \Delta q, \quad (16)$$

where  $\Delta q$  is the energy transfer between matter and neutrinos. If we are not too strict about where in space the energy transfer between matter and neutrinos takes place (for neutrino-electron scattering rather along one of the trajectories in Fig. 7 than in one and the same fluid element), one may simply set  $\Delta q = \Delta Y_e E_\nu^{\text{escape}}$  where  $E_\nu^{\text{escape}}$  is the average energy of the neutrinos when they escape the star [7]. This leads to the following expression for the entropy change (16):

$$T\Delta s = -\Delta Y_e (\mu_e - \mu_n + \mu_p - E_\nu^{\text{escape}}). \quad (17)$$

Figure 7 now illustrates, that up to a density of  $2 \times 10^{11}$  g/cm<sup>3</sup> we find  $E_\nu^{\text{escape}} > \mu_e - \mu_n + \mu_p$ . The entropy in this regime is decreasing. Therefore, also the entropy might slightly contribute to the convergence to a "norm" trajectory during the deleptonization: If a fluid element in one model has a higher temperature than in another model, more free protons are available for electron capture and the fluid element cools more rapidly toward the temperature in the other model. We also note that in this regime electron capture on nuclei produces neutrinos with lower escape energies and therefore contributes less to an entropy decrease than electron capture on free protons [111]. Between  $\rho = 2 \times 10^{11}$  g/cm<sup>3</sup> and  $\rho = 2 \times 10^{12}$  g/cm<sup>3</sup>, Fig. 7 indicates that  $E_\nu^{\text{escape}} < \mu_e - \mu_n + \mu_p$  such that the entropy increases because a part of the locally emitted neutrino energy is returned to the fluid by the thermalization of the neutrino. At even higher densities, only the thermalization down to the neutrino chemical potential occurs on a fast time scale such that fast electron fraction changes do no longer cause entropy changes because of  $\mu_\nu = \mu_e - \mu_n + \mu_p$ . The energy difference between  $\mu_\nu$  and  $E_\nu^{\text{escape}}$  is only returned to the fluid on the much longer diffusion time scale relevant for changes of the lepton fraction  $\Delta Y_\ell$ . These expectations are consistent with the actual entropy evolution at the center shown in Fig. 10.

### 3.3 Electron capture rates

Calculations of the reaction rate for electron capture in the collapsing core requires two components: the appropriate electron capture reaction rates and the knowledge of the nuclear composition. The coupling of electron capture rates to energy-dependent neutrino transport adds an additional requirement: information about the spectra of emitted neutrinos. These spectra can be parametrized using the prescription of Ref. [112]. During the collapse most of the collapsing matter survives in heavy nuclei as the entropy is rather low [44].  $Y_e$  decreases during the collapse due to electron capture, making the matter composition more neutron rich and hence favoring increasingly heavy nuclei. Unlike in stellar evolution and supernova nucleosynthesis simulations, where the nuclear composition is tracked in detail via a reaction network [1,113], the composition used in supernova simulations is calculated by the equation

of state, which assumes nuclear statistical equilibrium (NSE). Typically, the information about the nuclear composition provided by the equation of state is limited to the mass fractions of free neutrons and protons,  $\alpha$  particles and the sum of all heavy nuclei, as well as the identity of an average heavy nucleus, calculated either in the liquid drop framework [89] or based on a relativistic mean field model [114,115]. It should be noted that the most abundant nucleus is not necessarily the nucleus which dominate electron capture during the infall phase. For the evaluation of reaction rates on nuclei, due to the dependence on nuclear structure effects, a single nucleus approximation is not sufficient. It must be replaced by an ensemble average. Figure 8 shows the typical nuclear abundances [116] at two different conditions taken from a collapse trajectory from Ref. [117]. Before discussing how the detailed abundance information can be implemented in collapse simulations we briefly review the foundation for the calculation of electron capture rates during the infall phase.

Traditionally, in collapse simulations the treatment of electron capture on nuclei is schematic and rather simplistic. The nuclear structure required to derive the capture rate is then described solely on the basis of an independent-particle model for iron-range nuclei, i.e., considering only Gamow-Teller transitions from  $f_{7/2}$  protons to  $f_{5/2}$  neutrons [44,2,119,3]. In particular, this model predicts that electron capture vanishes for nuclei with neutron number  $N \geq 40$ , arguing that Gamow-Teller transitions are blocked due to the Pauli principle, as all possible final neutron orbitals are already occupied in nuclei with  $N \geq 40$  [106]. These nuclei dominate the composition for densities larger than a few  $10^{10}$  g cm<sup>3</sup>. As a consequence of the model applied in previous collapse simulations, electron capture on nuclei ceases at these densities and the capture is entirely due to free protons. It has been pointed out [107] that this picture is too simple and that the blocking of the Gamow-Teller transitions will be overcome by thermal excitations which either moves protons into the  $g_{9/2}$  orbit or removes neutrons from the  $pf$ -shell, in both ways unblocking the GT transitions. According to the work of Ref. [107], due to “thermal unblocking” GT transitions dominate again for temperatures of the order of 1.5 MeV. A more important unblocking effect, which is already relevant at lower temperatures is expected from the residual interaction which will mix the  $g_{9/2}$  and higher orbitals with the  $pf$  shell [120,21].

The calculation of electron capture on nuclei during the collapse phase requires a model that is able to describe the correlations and at the same time the high density of levels that can be thermally populated at moderate excitation energies. Direct shell-model diagonalizations are not yet possible due to the large model spaces involved. The calculations can be done using the Shell Model Monte Carlo approach [121] which allows for the calculation of nuclear properties at finite temperature in unprecedentedly large model spaces. This model complemented with Random Phase Approximation calculations for the computation of the transitions necessary for the determination of the electron

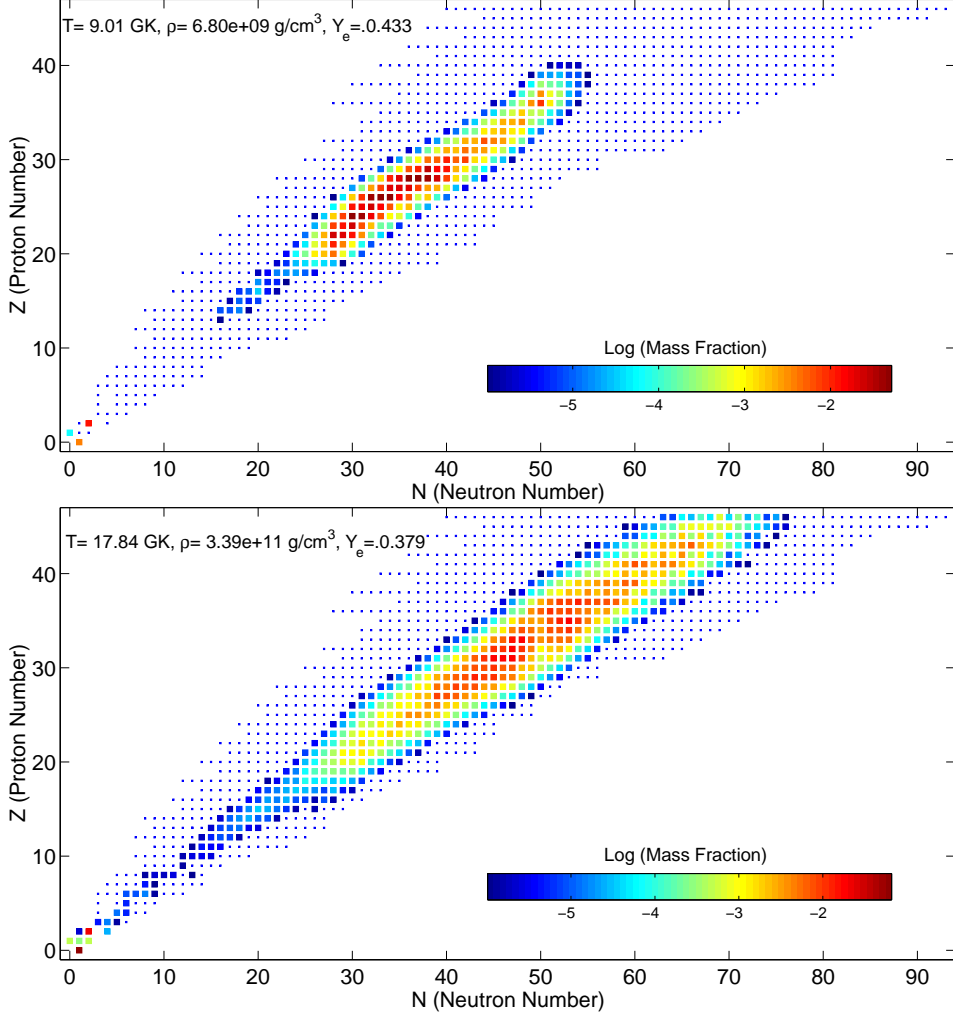


Fig. 8. Abundances of nuclei for two set of conditions during the collapse. The upper panel represents typical conditions during the early collapse while the lower panel shows conditions near to neutrino trapping. A Saha-like NSE code has been used in the calculation of the abundances [118] (Adapted from [116]).

capture rate has been used recently for the calculation of the relevant rates for nuclei in the mass range  $A = 65\text{--}112$  [21]. Currently electron capture rates are available for all the nuclei in the mass range  $A = 17\text{--}112$  and for the temperatures and densities relevant for the collapse [47,74,75,21,122].

Figure 9 compares the electron capture rates for free protons and selected nuclei along a stellar trajectory taken from [28]. These nuclei are abundant at different stages of the collapse. For all the nuclei, the rates are dominated by GT transitions at low densities, while forbidden transitions contribute sizably for  $\rho \gtrsim 10^{11} \text{ g cm}^{-3}$ . The electron chemical potential  $\mu_e$  and the reaction  $Q$  value are the two important energy scales of the capture process. (They are shown on the right panel of figure 9.) The  $Q$ -value dependence of the capture

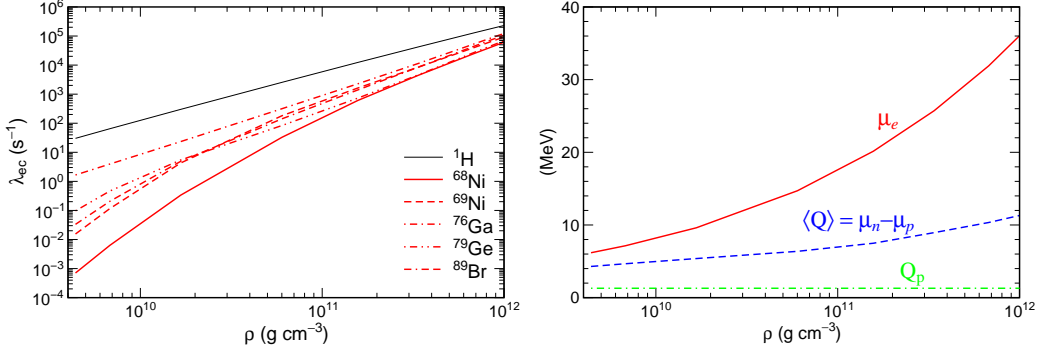


Fig. 9. (left panel) Comparison of the electron capture rates on free protons and selected nuclei as function of density chemical potential along a stellar collapse trajectory taken from [28]. (right panel) energy scales relevant for the determination of the electron capture rates.  $\mu_e$  is the electron chemical potential.  $\langle Q \rangle$  and  $Q_p$  are the average  $Q$  value for electron capture on nuclei and protons respectively.

rate can be well approximated by [48]:

$$\lambda = \frac{(\ln 2)B}{K} \left( \frac{T}{m_e c^2} \right)^5 \left[ F_4(\eta) + 2\chi F_3(\eta) + \chi^2 F_2(\eta) \right], \quad (18)$$

where  $\chi = Q/T$ ,  $\eta = (\mu_e - Q)/T$ ,  $K = 6146$  s, and  $B$  represents a typical (Gamow-Teller plus forbidden) matrix element. The quantities  $F_k$  are the relativistic Fermi integrals of order  $k$ <sup>1</sup>.  $Q$  represents the effective  $Q$ -value for the capture rate including thermal effects. In equation (18), we use the convention that  $Q$  is positive for capture on neutron rich nuclei and protons. For low densities ( $\lesssim 10^{10} \text{ g cm}^{-3}$ ),  $\mu_e \approx Q$  and the term  $F_2$  dominates. The rate is then larger for the nuclei with smaller  $Q$  values. For intermediate densities ( $10^{10}$ – $10^{11} \text{ g cm}^{-3}$ ), the term  $F_3$  dominates and the rate still has some dependence on the  $Q$ -value. For high densities ( $\gtrsim 10^{11} \text{ g cm}^{-3}$ ),  $\mu_e \gg Q$  so that the term  $F_4$  dominates and the rate becomes independent of the  $Q$ -value, depending only on the total GT strength, but not its detailed distribution.

According to figure 9, the electron capture rate on a proton is larger than that for individual nuclei. However, this is misleading as the low entropy keeps the protons significantly less abundant than heavy nuclei during the collapse. Simulations of core collapse require then the knowledge of the detailed abundances of all the nuclei present. As the commonly used equations of state [89,114,115] do not provide this detailed information, a Saha-like NSE was used for the calculation of the abundances in refs. [21,96]. Once the abundances are considered the reaction rate for electron capture on heavy nuclei ( $R_h = \sum_i Y_i \lambda_i$ , where the sum runs over all the nuclei present and  $Y_i$  denotes the number abundance of species  $i$ ) dominates over the one of protons ( $R_p = Y_p \lambda_p$ ) by roughly an order of magnitude throughout the collapse [21,96]. The first sim-

<sup>1</sup> The fermi integrals are defined by:  $F_k(\eta) = \int_0^\infty dx x^k / (1 + \exp(x - \eta))$

ulations that considered electron capture on nuclei with  $N \geq 40$  were probably the ones of Ref. [111]. These authors determined the electron-capture rate by detailed balance from their computed  $\nu_e$  absorption rate. This corresponds to electron capture on the thermally populated Fermi and  $GT_-$  resonances in the parent nucleus shown in figure 1 (also called backresonances according to the notation of [45]) that decay to the daughter ground state. This backresonance contribution is in general, depending on the nucleus, a factor between 10 and 100 smaller than the direct transition from the parent ground state to the daughter Gamow-Teller resonance. This explains why, in contrary to the results of refs. [21,96], electron capture on nuclei was too small in Ref. [111] so that it was concluded that electron capture on protons dominates over capture on nuclei.

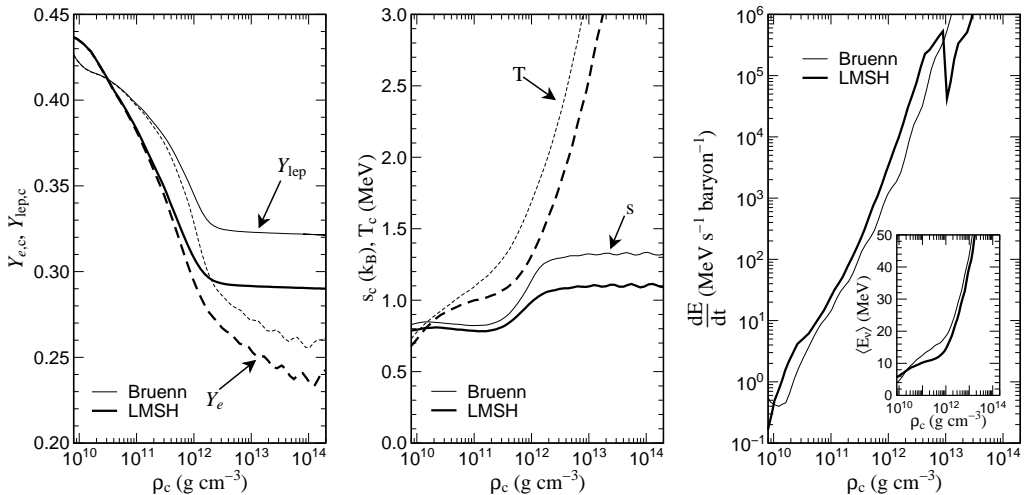


Fig. 10. Comparison of the evolution of several quantities at the center of a  $15 M_{\odot}$ :  $Y_e$  is the number of electrons per baryon,  $Y_{\text{lep}}$  is the number of leptons per baryon  $s$  is the entropy per baryon,  $T$  is the temperature,  $dE/dt$  is the neutrino energy emission rate per baryon,  $\langle E_{\nu} \rangle$  is the average energy of the emitted neutrinos. An abrupt change in the emission occurs when the domain where the LMSH rates are specified is exceeded at a density of  $10^{13} \text{ g/cm}^3$ . The initial presupernova model was taken from [76]. The thin line is a simulation using the Bruenn parametrization [2] while the thick line uses the LMSH rate set (see text). Both models include the general relativistic effects discussed in section 3.1 and were calculated by the Garching collaboration (Courtesy of M. Rampp and H.-Th. Janka).

The effects of the more realistic implementation of electron capture on heavy nuclei have been evaluated as described above in independent self-consistent neutrino radiation hydrodynamics simulations by the Oak Ridge and Garching collaborations [96,123]. The results obtained by the Garching collaboration are shown in Fig. 10 [123] for the evolution of several quantities at the center of a  $15 M_{\odot}$  star using the standard treatment of Bruenn [2] and the new rates for heavy nuclei (denoted LMSH). With the improved treatment of electron capture rate on heavy nuclei the total electron capture rate (heavy nuclei plus protons) is larger than in the Bruenn treatment resulting in smaller  $Y_e$

and  $Y_{\text{lepton}}$  values. The left panel shows the evolution of these quantities at the center of the star as functions of the increasing density during collapse. The small oscillations in the trajectories above  $5 \times 10^{12} \text{ g/cm}^3$  are due to the same numerical effect of finite energy resolution under neutrino-degenerate conditions that we have already seen in Fig. 7. The panel demonstrates that the Bruenn treatment leads to a faster deleptonization for representative nuclei with  $N < 40$  (at low density) while this channel is blocked afterwards such that the further deleptonization is delayed and falls short of the LMSH treatment where electron captures on nuclei continue. The panel on the right shows the energy per baryon and second emitted in neutrinos at the center of the star. The inset shows the mean energy of the produced neutrinos. With the LMSH treatment, more neutrinos are produced with lower mean energy than with the Bruenn treatment. The center panel shows the entropy and temperature evolution at the center of the star. The general entropy trajectory is consistent with the discussion following Eq. (17). The entropy is slowly descending at low density because  $E_{\nu}^{\text{escape}}$  is larger than  $\mu_e - \mu_n + \mu_p$ . As soon as neutrino-electron scattering becomes effective to downscatter neutrinos,  $E_{\nu}^{\text{escape}}$  falls below above chemical potential difference (see Fig. 7, left panel) and the transferred heat starts to increase the fluid entropy until the diffusion time scale becomes larger than the dynamical time scale. With the LMSH treatment one would now be tempted to expect that the central entropy would rise to larger values than with the Bruenn treatment because the deleptonization  $\Delta Y_e$  in Eq. (17) increases according to the values shown in the left panel. Additionally the neutrinos are emitted with lower energies so that  $E_{\nu}^{\text{escape}}$  might also decrease somewhat to favor a steep entropy increase. However, the center panel shows clearly that the LMSH treatment leads to smaller central entropies. In order to better illustrate speculations about the possible reasons of this interesting result, we performed a simple test calculation for a comparison in Fig. 7 where one state in the neutron  $f_{5/2}$  orbit was kept unblocked in the Bruenn treatment. One immediately sees in the right panel that the average energy of emitted neutrinos (asterisks) is lower than with the Bruenn treatment and that less neutrino-electron scattering takes place before the escape. This difference in the thermalization path reduces the diffusion time. For an understanding of the entropy differences however, it is crucial to realize that the difference in the deleptonization between the Bruenn and LMSH rates occurs *before* the density is reached where the entropy rises. We define a first phase, reaching from low densities to  $\rho = 3 \times 10^{10} \text{ g/cm}^3$ , so that the net deleptonization for the two rates is exactly the same (left panel in Fig. 10). As both rates include electron capture on nuclei at these densities, Eq. (17) does not predict noticeable differences in the entropy evolution. In a second phase, reaching from  $\rho = 3 \times 10^{10}$  to  $\rho = 2 \times 10^{11} \text{ g/cm}^3$ , electron capture on nuclei is blocked in the Bruenn treatment and a significantly smaller net deleptonization  $-\Delta Y_e$  in Eq. (17) occurs than with the LMSH rates. However, Fig. 7 shows that in this phase the second factor,  $\mu_e - \mu_n + \mu_p - E_{\nu}^{\text{escape}}$ , is much smaller than in the LMSH case because electron capture on free protons produces neutrinos



with larger escape energies  $E_\nu^{\text{escape}}$  than electron capture on nuclei. The two effects cancel in the evaluation of  $T\Delta s$  in Eq. (17) and the entropy evolution in this phase is again similar with both sets of rates. Now, in the third phase, reaching from  $\rho = 2 \times 10^{11}$  to  $\rho = 2 \times 10^{12}$  g/cm<sup>3</sup>, there is no significant difference in the net deleptonization for the two cases anymore,  $-\Delta Y_e \sim 0.09$ , but the lower  $Y_e$  values increase the difference between the neutron and proton chemical potentials,  $\mu_n - \mu_p$ , in the LMSH case. On the other hand, the energy of escaping neutrinos,  $E_\nu^{\text{escape}}$ , decreases, but only about half as much. Both effects together cause a difference  $\sim 2$  MeV in the factor  $\mu_e - \mu_n + \mu_p - E_\nu^{\text{escape}}$ , which seems consistent with the displayed difference in the entropy evolution before trapping in the center panel of Fig. 10. The increased neutron to proton asymmetry in the LMSH case also leads to heavier nuclei with higher opacities for a given density and neutrino energy (see section 3.5). This shifts the deleptonization region to slightly lower densities where the energy scales are smaller. This might also contribute to the entropy difference.

### 3.4 Inelastic Neutrino-Nucleus Interactions

Although the classical thermalization mechanism for the neutrinos proceeds through inelastic scattering on electrons, Eq. (8), neutrino-induced reactions on nuclei can also occur [124,111]. Charged-current ( $\nu_e, e^-$ ) reactions on nuclei are unimportant during the collapse compared with inelastic neutrino-electron scattering due to the strong Pauli blocking of the final electron phase space [111]. This is so even if finite temperature effects are considered [125].

However, according to Ref. [111], neutrino-nucleus inelastic scattering plays an as important role as neutrino-electron scattering. The influence of finite temperature was studied in Ref. [126] using an independent particle model. More recently, neutrino cross sections for finite temperature have been calculated using shell-model GT distributions [127,128]. This approach has been validated for the calculation of neutrino-nucleus inelastic scattering against high resolution magnetic dipole data [129]. Finite temperature enhances the cross section for low energy neutrinos. This is due to the fact that at finite temperatures the initial nucleus can reside in excited states which can be connected to the ground state by large GT matrix elements. These states are deexcited by inelastic neutrino scattering. In this case, contrarily to what happens in neutrino-electron scattering, the final neutrino energy is larger than the initial. Currently no hydrodynamical collapse simulations are available that include both electron capture on nuclei and neutrino-nucleus inelastic scattering. Nevertheless, the simple fact that the cross sections are of similar magnitude than scattering on electrons [127] suggest their inclusion in supernova neutrino transport codes.

Other neutrino processes such as nuclear deexcitation by neutrino pair production, Eq. (11), have been discussed in Ref. [126], but the estimated rates are probably too small for these processes to be important during the collapse.

### 3.5 Neutrino opacities

After the detailed description of the new electron capture rates in section 3.3 and the emphasis of the importance of neutrino thermalization in sections 3.2 and 3.4, we conclude the discussion of nuclear input for core-collapse models with a few pointers to the third relevant ingredient: neutrino opacities. The fundamental neutrino opacity in core collapse is provided by neutrino scattering on nucleons. Depending on the distribution of the nucleons in space and the wavelength of the neutrinos, various important coherence effects can occur: Most important during collapse is the binding of nucleons in nuclei with a density contrast of several orders of magnitude to the surrounding nucleon gas. For elastic neutrino-nucleus scattering one usually makes the simplifying assumption that the nucleus has a  $J = 0^+$  spin/parity assignment. This is appropriate for the ground state of even-even nuclei. The scattering process is then restricted to the Fermi part of the neutral current (pure vector coupling) [130,131]. Because of coherent scattering, the cross section scales with  $A^2$ , except from a correction  $\sim (N - Z)/A$  arising from the neutron excess. This assumption is, in principle, not correct for the ground states of odd- $A$  and odd-odd nuclei and for all nuclei at finite temperature, as then  $J \geq 0$  and the cross section will also have an axial-vector Gamow-Teller contribution. However, the relevant  $GT_0$  strength is not concentrated in one state, but rather fragmented over many nuclear levels. Thus, one can expect that the GT contributions to the elastic neutrino-nucleus cross sections are in general small enough to be neglected. A useful comparison of inverse mean free paths at the important density  $\rho = 10^{12}$  g/cm<sup>3</sup> is given in [132]. It is found that  $\lambda_{\nu+n}/\lambda_{\nu+A} \sim 3 \times 10^{-2}$ ,  $\lambda_{\nu+e}/\lambda_{\nu+A} \sim 2.5 \times 10^{-2}$ ,  $\lambda_{\nu+He}/\lambda_{\nu+A} \sim 10^{-4}$ , and  $\lambda_{\nu+p}/\lambda_{\nu+A} \sim 5 \times 10^{-5}$ .

Further corrections are necessary: with an increasing ratio between the Coulomb potential of the positively charged ions and their thermal energy, the average separation between nuclei will more strongly peak around the value of most efficient packing. The neutrino opacities are then to be corrected by an ion-ion correlation function  $\langle S_{ion}(E_\nu) \rangle < 1$  [133,134,135]. Its consideration in core collapse simulations lowers the trapped lepton fraction at bounce by 0.015 and increases the central entropy per baryon by 0.12 kB [132]. It is found that the sizable entropy increase is not only due to the increased deleptonization, but also to the fact that the correlation effect is most pronounced for the low energy neutrinos with a long wavelength. Hence the entropy increase is additionally supported by a decrease of  $E_\nu^{\text{escape}}$  in the discussion following Eq. (17).

As current core collapse models proceed toward including the full ensemble of nuclei instead of just a representative nucleus (cf. Fig. 8), it becomes rather non-trivial how to adequately determine correlation effects in the ion mixture, see for example [134,136].

The situation is even more interesting in the phase transition from isolated nuclei to bulk nuclear matter where the nuclei or the holes inbetween them are strongly deformed. Various pasta-like shapes may be assumed. Correlation effects in this phase could also affect the neutrino opacities [99]. For an immediate effect on core collapse, however, it would be required that this “pasta-phase” would reach to fairly low densities in order to affect the opacities at the neutrinospheres where the neutrino luminosities and spectra are set (cf. Fig. 7).

A more detailed description of the neutrino opacities in nuclear matter is given elsewhere in this volume [6]. An extensive quantitative overview of the rates of most reactions has been provided in Ref. [111]. Useful fitformulae are collected in Ref. [134].

#### 4 Effects on the postbounce evolution

Stellar core collapse and supernova explosion have often been discussed as one and the same event. This view has also observationally been confirmed by the detection of few neutrinos from supernova 1987A [137,138,139]. The connection has further been nourished by the early theory of a prompt explosion mechanism where, as a consequence of bounce, a strong shock rushes through the outer core to eject the outer layers. However, we are not aware of any simulation with reasonable neutrino physics that would have predicted a prompt explosion since the Lattimer-Swesty equation of state [89] has become standard. In contrary, due to the stiff behaviour of the equation of state around nuclear density the initial shock is weak as discussed in section 3.1. Additionally it starts at a very deep mass coordinate because of the efficient deleptonization discussed in sections 3.2-3.3. In fact, recent spherically symmetric simulations of the postbounce evolution predict that the shock stalls already  $\sim 3$  ms after bounce, i.e. before or at the time the neutrino burst is launched from neutrino-transparent layers and  $\sim 40$  ms *before* a gain layer can develop for neutrino heating to become effective. Many publications of supernova models include figures with shock trajectories that show a continued expansion of the shock front to about 150 km at 100 ms after bounce. Note, however, that there is no valid concept of shock energy that reaches beyond the few milliseconds after which the shock has stalled. The continued expansion of the accretion front over at least 90% of the  $\sim 100$  ms interval is due to the accumulation of material on the protoneutron star: heavy nuclei from

the outer layers are accelerated in the gravitational potential until they fall upon the accretion front where their kinetic energy is converted into heat. The accretion front is displaced to a larger radius mainly by the increased volume of the accumulated hot and dissociated matter and not by shock energy.

The sophisticated nuclear physics required in core collapse models and the complicated dynamics in the ensuing supernova explosion suggest a point of view where the theory of core collapse may well be as detached from supernova explosions as, for example, the dynamics of star formation from stellar evolution. On the one hand, core collapse involves the nuclear and weak interaction physics of heavy nuclei under electron degenerate conditions in layers that are unstable to gravitational collapse. The supernova explosion, on the other hand, involves fundamentally multi-dimensional neutrino-radiation-hydrodynamics in hot dissociated matter that is in convective motion around a possibly magnetized compact object. Also the technical refinement of simulations of the collapse phase has always been roughly 10 years ahead of the corresponding simulations of the postbounce phase. Based on the current understanding, it would be an optimistic expectation that any very relevant change in one domain (core collapse) would automatically induce a revolution in the other (supernova explosion).

Important changes have been discovered in the core collapse event. In conventional simulations, electron capture on nuclei has been treated as blocked for nuclei with  $N > 40$ . Recent models that include realistic electron capture rates beyond this limit show that electron capture on these nuclei are not only relevant, but even provide the dominant channel for the deleptonization during collapse [21,96], with important consequences for core-bounce: In the interior of the protoneutron star the electron fraction is reduced by  $\sim 10\%$  when compared to models that don't include electron captures on nuclei. This change corresponds to a reduction of 20% in the mass of the homologous core and translates directly to a reduction of the mass interior to the point of shock formation. Moreover, the shock is launched with a  $\sim 15\%$  smaller velocity difference. The weaker shock with more iron core overlying it turns even earlier (and at a deeper mass coordinate) into an expanding accretion front than in models with "standard" physics. Furthermore, the improved treatment of electron capture also affects the outer layers where the average neutron number is well below  $N = 40$ . For these conditions the treatment of electron capture by Bruenn [2] results in more electron capture than with the shell-model based electron capture rates [20]. The smaller neutronization in the outer layers slows the collapse in these layers which further diminishes the growth of the electron capture rate. These changes delay the accretion of matter and reduce the ram pressure opposing the expansion of the accretion front. Both effects can modify the trajectory of the accretion front as a function of time.

In spherically symmetric simulations the accretion front reaches a maximum

expansion  $\sim 100$  ms after bounce when the compression of matter in the cooling region starts to exceed the volume of accumulated shock- and neutrino-heated matter at the accretion front. However, because the shock stalls within milliseconds in old and new models, the significant changes in the core collapse physics cannot dynamically push through to the explosion phase. Also the temporal variations in the accretion rate tend to average over  $\sim 100$  ms, so that the maximum radius in the postbounce expansion of the accretion front is not significantly sensitive to the improvements of the electron capture rates on nuclei. Nevertheless, core collapse still sets the stage for a delayed supernova explosion and several consequences of the nuclear physics during core collapse survive for a longer time than the often overemphasized shock dynamics, or are in principle directly observable.

Due to the extended accretion phase of delayed explosions, most if not all of the iron core is packed in the protoneutron star. Hence, differences in the physics of core collapse will most likely translate to differences in the interior of the protoneutron star. The deleptonization during collapse and the early shock energetics leave a clear imprint on the entropy profile at high densities. Indeed, models that include electron capture on nuclei show considerably different entropy and lepton fraction gradients when compared to standard treatments of electron capture [96]. These gradients are responsible for the location, extent and strength of the protoneutron star convection and other possible fluid instabilities. Seminal simulations by [140] favored a strong coupling between the protoneutron star interior and the exterior layers subject to neutrino heating. The equation of state used at that time suggested fluid instabilities which, implemented by a mixing-length approach in spherically symmetric simulations, supported the existence of delayed neutrino-driven supernova explosions. Analytical investigations based on the Lattimer-Swesty equation of state [141] and recent numerical simulations [36] find convectively stable neutrinospheres that efficiently block a rapid release of neutrinos from the convectively unstable protoneutron star interior. But a change in the nuclear input physics always carries the potential to affect the structure of the protoneutron star in a way that possibly revives the strong coupling of its interior to the outer layers. A recent detailed investigation of the protoneutron star stability is given in Ref. [37].

The neutrino luminosities and energies during collapse, bounce, and the interesting time of the launch of the electron neutrino burst are in principle more directly observable. Figure 11 shows the luminosity and root-mean-square energy of the emitted electron neutrinos and antineutrinos (sampled at 500 km radius in the comoving coordinate frame) between 100 ms before bounce and 100 ms after bounce. One model (thick lines) includes electron captures on nuclei (LMSH) and the other (thin lines) uses the standard Bruenn treatment. The luminosity shows a clear delay (2 ms) in the breakout burst due to a deeper launch of the shock in the LMSH case. Consistent with the depen-

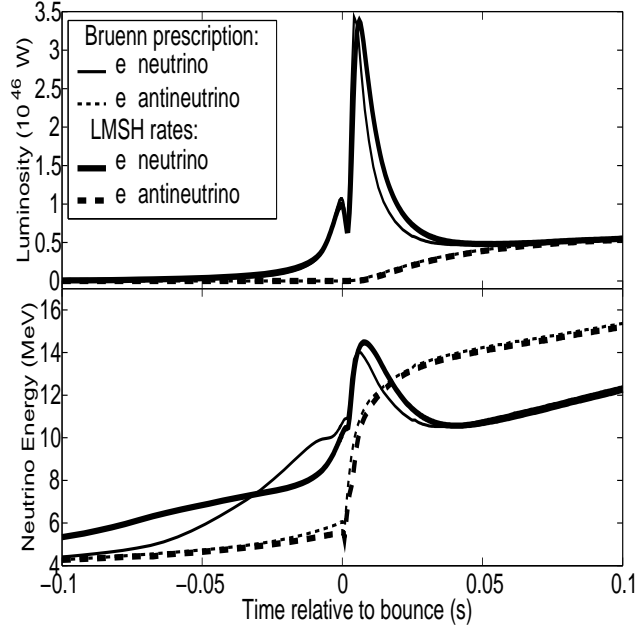


Fig. 11. The neutrino luminosity and root-mean-square energy (at 500 km) as a function of time from bounce for a  $15 M_{\odot}$  model. The thin lines show this evolution for a simulation using the Bruenn parametrization [2], while the thick lines show this evolution for a simulation using the LMSH rates [21,96]. The solid lines correspond to electron type neutrinos; the dashed lines correspond to electron type antineutrinos. Both cases were calculated in a general relativistic model by the Oak-Ridge collaboration (adapted from [96]).

dence of the neutrino burst intensity on the shock strength [31], the LMSH neutrino burst is also more extended in time. Before bounce the neutrino luminosities are similar but the average energies are smaller in the LMSH case due to the larger  $Q$ -values involved for electron capture on nuclei as discussed above. After bounce, during the first 50 ms the LMSH model emits  $\sim 15\%$  more energy than the Bruenn model. This is mainly the result of a larger mean electron neutrino energy in the LMSH model due to a deeper and hotter neutrinosphere [96].

Neutrino-induced reactions on nuclei are expected to contribute only modestly to the shock revival, due to the small abundance of nuclei during this phase. It has been suggested that the shock revival can be aided by “preheating” of matter ahead of the shock by absorption of electron neutrinos emitted in the breakout burst [124]. These neutrinos can partly dissociate the matter, mainly iron and silicon isotopes, before the arrival of the shock. The early explorations of Ref. [111] found no significant preheating of unshocked matter. Once the matter is processed by the shock, large amounts of  ${}^4\text{He}$  are present just below the stagnated shock. The possibility of reheating this material by inelastic  $\nu_x$ - ${}^4\text{He}$  scattering, where  $\nu_x$  denotes muon or tau neutrino and antineutrino, or heating the material ahead of the shock by  $\nu_x$ -nucleus inelastic scattering was

also investigated in Ref. [111] with no major effect found. Nevertheless, only recently reliable neutrino-nucleus cross sections have become available [128] that allow for a complete study of the influence of neutrino-nucleus scattering both in the collapse and postbounce evolution.

## 5 Conclusions

Core-collapse supernovae present a rich interplay between nuclear physics and neutrino radiation (magneto-)hydrodynamics. Nuclear physics sets the scene in which different hydrodynamical instabilities could develop that eventually may produce robust explosions by the neutrino-driven mechanism (see for example refs. [142,143,39] for recent overviews over the activities of collaborations engaging in accurate neutrino transport). The nuclear equation of state governs stellar core collapse, core bounce and neutron star formation. The complicated interplay between deleptonization, neutrino thermalization, and diffusion based on different weak interaction processes—the most important of them is electron capture on nuclei—determine the collapse dynamics, the position of shock formation and the structure of the layers into which the shock expands. Advances in the calculations of these processes coupled to improvements in one and multi-dimensional accurate neutrino transport simulations has allowed to gain further insight to the physics of the collapsing core. Future advances on the nuclear physics side should be guided by the advent of new radiative-ion beam facilities that will help to constrain the nuclear models used for the determination of the equation of state and the different nuclear weak-interaction processes. These advances coupled to current efforts to develop multidimensional magneto-hydrodynamical codes with accurate neutrino transport will foster a definitive and quantitative understanding of supernova explosions.

## References

- [1] S. E. Woosley, in *Nucleosynthesis and Chemical Evolution*, edited by B. Hauck, A. Maeder, G. Meynet, vol. 16 of *Saas-Fee Advanced Courses* (Geneva Observatory, 1986), pp. 1–195.
- [2] S. W. Bruenn, *Astrophys. J. Suppl.* **58** (1985) 771.
- [3] A. Mezzacappa, S. W. Bruenn, *Astrophys. J.* **410** (1993) 740.
- [4] M. Rampp, H.-T. Janka, *Astron. & Astrophys.* **396** (2002) 361.
- [5] K. Langanke, G. Martínez-Pinedo, *Rev. Mod. Phys.* **75** (2003) 819.

- [6] A. Burrows, S. Reddy, T. A. Thompson, Nucl. Phys. A (2004), [astro-ph/0404432](#).
- [7] H. A. Bethe, Rev. Mod. Phys. **62** (1990) 801.
- [8] S. Hannestad, G. Raffelt, Astrophys. J. **507** (1998) 339.
- [9] T. A. Thompson, A. Burrows, J. E. Horvath, Phys. Rev. C **62** (2000) 035802.
- [10] J. R. Bond, Ph.D. thesis (1979).
- [11] R. Buras, H. Janka, M. T. Keil, G. G. Raffelt, M. Rampp, Astrophys. J. **587** (2003) 320.
- [12] M. T. Keil, G. G. Raffelt, H. Janka, Astrophys. J. **590** (2003) 971.
- [13] E. S. Myra, S. A. Bludman, Astrophys. J. **340** (1989) 384.
- [14] S. W. Bruenn, Astrophys. J. **340** (1989) 955.
- [15] S. W. Bruenn, Astrophys. J. **341** (1989) 385.
- [16] J. Cooperstein, Nucl. Phys. A **556** (1993) 237.
- [17] J. R. Wilson, R. W. Mayle, Phys. Repts. **227** (1993) 97.
- [18] M. Liebendörfer, A. Mezzacappa, F.-K. Thielemann, O. E. Bronson Messer, W. Raphael Hix, S. W. Bruenn, Phys. Rev. D **63** (2001) 103004.
- [19] E. Caurier, G. Martínez-Pinedo, F. Nowacki, A. Poves, A. P. Zuker, Rev. Mod. Phys. (2004), in press, [nucl-th/0402046](#).
- [20] K. Langanke, G. Martínez-Pinedo, Nucl. Phys. A **673** (2000) 481.
- [21] K. Langanke, *et al.*, Phys. Rev. Lett. **90** (2003) 241102.
- [22] E. Caurier, K. Langanke, G. Martínez-Pinedo, F. Nowacki, Nucl. Phys. A **653** (1999) 439.
- [23] B. M. Sherrill, *et al.*, Nucl. Instrum. Methods Phys. Res., Sect. A **432** (1999) 299.
- [24] I. Daito, *et al.*, Phys. Lett. B **418** (1998) 27.
- [25] H. Ohnuma, *et al.*, Phys. Rev. C **47** (1993) 648.
- [26] H. M. Xu, *et al.*, Phys. Rev. C **52** (1995) R1161.
- [27] M. Rampp, H.-T. Janka, Astrophys. J. **539** (2000) L33.
- [28] A. Mezzacappa, M. Liebendörfer, O. E. Bronson Messer, W. Raphael Hix, F.-K. Thielemann, S. W. Bruenn, Phys. Rev. Lett. **86** (2001) 1935.
- [29] S. W. Bruenn, K. R. De Nisco, A. Mezzacappa, Astrophys. J. **560** (2001) 326.
- [30] T. A. Thompson, A. Burrows, P. A. Pinto, Astrophys. J. **592** (2003) 434.



- [31] M. Liebendörfer, M. Rampp, H.-T. Janka, A. Mezzacappa (2004), to be published in *Astrophys. J.*, [astro-ph/0310663](#).
- [32] M. Herant, W. Benz, W. R. Hix, C. L. Fryer, S. A. Colgate, *Astrophys. J.* **435** (1994) 339.
- [33] A. Burrows, J. Hayes, B. A. Fryxell, *Astrophys. J.* **450** (1995) 830.
- [34] H.-T. Janka, E. Müller, *Astron. & Astrophys.* **306** (1996) 167.
- [35] A. Mezzacappa, *et al.*, *Astrophys. J.* **495** (1998) 911.
- [36] R. Buras, M. Rampp, H.-T. Janka, K. Kifonidis, *Phys. Rev. Lett.* **90** (2003) (24) 241101.
- [37] S. W. Bruenn, E. A. Raley, A. Mezzacappa (2004), [astro-ph/0404099](#).
- [38] J. M. Blondin, A. Mezzacappa, C. DeMarino, *Astrophys. J.* **584** (2003) 971.
- [39] H.-T. Janka, R. Buras, F. S. Kitaura, A. Marek, M. Rampp, L. Scheck (2004), to be published in *Nucl. Phys. A*, [astro-ph/0411347](#).
- [40] C. Thompson, *Astrophys. J.* **534** (2000) 915.
- [41] S. Akiyama, J. C. Wheeler, D. L. Meier, I. Lichtenstadt, *Astrophys. J.* **584** (2003) 954.
- [42] T. A. Thompson, E. Quataert, A. Burrows (2004), to be published in *Astrophys. J.*, [astro-ph/0403224](#).
- [43] K. Kotake, H. Sawai, S. Yamada, K. Sato, *Astrophys. J.* **608** (2004) 391.
- [44] H. A. Bethe, G. E. Brown, J. Applegate, J. M. Lattimer, *Nucl. Phys. A* **324** (1979) 487.
- [45] G. M. Fuller, W. A. Fowler, M. J. Newman, *Astrophys. J. Suppl.* **42** (1980) 447.
- [46] G. M. Fuller, W. A. Fowler, M. J. Newman, *Astrophys. J.* **252** (1982) 715.
- [47] G. M. Fuller, W. A. Fowler, M. J. Newman, *Astrophys. J. Suppl.* **48** (1982) 279.
- [48] G. M. Fuller, W. A. Fowler, M. J. Newman, *Astrophys. J.* **293** (1985) 1.
- [49] C. J. Hansen, Ph.D. thesis, Yale University (1966).
- [50] C. J. Hansen, *Astrophys. Space Sci.* **1** (1968) 499.
- [51] T. Mazurek, Ph.D. thesis, Yeshiva University (1973).
- [52] T. Mazurek, J. W. Truran, A. G. W. Cameron, *Astrophys. Space Sci.* **27** (1974) 161.
- [53] K. Takahashi, M. Yamada, T. Kondoh, *At. Data. Nucl. Data Tables* **12** (1973) 101.

- [54] K. Takahashi, M. F. El Eid, W. Hillebrandt, *Astron. & Astrophys.* **67** (1978) 185.
- [55] M. B. Aufderheide, I. Fushiki, S. E. Woosley, D. H. Hartmann, *Astrophys. J. Suppl.* **91** (1994) 389.
- [56] C. Bäumler, *et al.*, *Phys. Rev. C* **68** (2003) 031303.
- [57] A. L. Williams, *et al.*, *Phys. Rev. C* **51** (1995) 1144.
- [58] S. El-Kateb, *et al.*, *Phys. Rev. C* **49** (1994) 3128.
- [59] W. P. Alford, *et al.*, *Phys. Rev. C* **48** (1993) 2818.
- [60] W. P. Alford, *et al.*, *Nucl. Phys. A* **514** (1990) 49.
- [61] M. C. Vetterli, *et al.*, *Phys. Rev. C* **40** (1990) 559.
- [62] J. Rapaport, *et al.*, *Nucl. Phys. A* **410** (1983) 371.
- [63] B. D. Anderson, C. Lebo, A. R. Baldwin, T. Chittrakarn, R. Madey, J. W. Watson, *Phys. Rev. C* **41** (1990) 1474.
- [64] B. D. Anderson, *et al.*, *Phys. Rev. C* **31** (1985) 1161.
- [65] C. D. Goodman, *et al.*, *Phys. Rev. Lett.* **44** (1980) 1755.
- [66] F. Osterfeld, *Rev. Mod. Phys.* **64** (1992) 491.
- [67] B. A. Brown, B. H. Wildenthal, *Annu. Rev. Nucl. Part. Sci.* **38** (1988) 29.
- [68] M. Hagemann, *et al.*, *Phys. Lett. B* **579** (2004) 251.
- [69] A. Poves, J. Sánchez-Solano, E. Caurier, F. Nowacki, *Nucl. Phys. A* **694** (2001) 157.
- [70] M. B. Aufderheide, *Nucl. Phys. A* **526** (1991) 161.
- [71] M. B. Aufderheide, S. D. Bloom, G. J. Mathews, D. A. Resler, *Phys. Rev. C* **53** (1996) 3139.
- [72] M. B. Aufderheide, S. D. Bloom, D. A. Ressler, G. J. Mathews, *Phys. Rev. C* **47** (1993) 2961.
- [73] M. B. Aufderheide, S. D. Bloom, D. A. Ressler, G. J. Mathews, *Phys. Rev. C* **48** (1993) 1677.
- [74] T. Oda, M. Hino, K. Muto, M. Takahara, K. Sato, *At. Data Nucl. Data Tables* **56** (1994) 231.
- [75] K. Langanke, G. Martínez-Pinedo, *At. Data. Nucl. Data Tables* **79** (2001) 1.
- [76] A. Heger, K. Langanke, G. Martínez-Pinedo, S. E. Woosley, *Phys. Rev. Lett.* **86** (2001) 1678.
- [77] A. Heger, S. E. Woosley, G. Martínez-Pinedo, K. Langanke, *Astrophys. J.* **560** (2001) 307.

- [78] S. E. Woosley, T. A. Weaver, *Astrophys. J. Suppl.* **101** (1995) 181.
- [79] M. B. Aufderheide, I. Fushiki, G. M. Fuller, T. A. Weaver, *Astrophys. J.* **424** (1994) 257.
- [80] S. E. Woosley, A. Heger, T. A. Weaver, *Rev. Mod. Phys.* **74** (2002) 1015.
- [81] C. Fröhlich, *et al.* (2004) astro-ph/0408067, submitted to *Nucl. Phys. A*.
- [82] J. Pruet, S. E. Woosley, R. Buras, H.-T. Janka, R. D. Hoffman (2004), astro-ph/0409446.
- [83] C. Fröhlich, *et al.* (2004), submitted to the *Astrophys. J.*, astro-ph/0410208.
- [84] K. Kifonidis, T. Plewa, H.-T. Janka, E. Müller, *Astrophys. J.* **531** (2000) L123.
- [85] D. K. Nadyozhin, *Ap. Space Sci.* **51** (1977) 283.
- [86] R. I. Epstein, in *ASSL Vol. 66: Supernovae* (1977), p. 183.
- [87] W. D. Arnett, *Astrophys. J.* **218** (1977) 815.
- [88] K. A. van Riper, W. D. Arnett, *Astrophys. J. Suppl.* **225** (1978) L129.
- [89] J. M. Lattimer, F. D. Swesty, *Nucl. Phys. A* **535** (1991) 331.
- [90] P. Goldreich, S. V. Weber, *Astrophys. J.* **238** (1980) 991.
- [91] A. Yahil, *Astrophys. J.* **265** (1983) 1047.
- [92] S. L. Shapiro, S. A. Teukolsky, *Black Holes White Dwarfs and Neutron Stars: The Physics of Compact Objects* (Wiley-Interscience, New York, 1983).
- [93] M. Takahara, K. Sato, *Progress of Theoretical Physics* **72** (1984) 978.
- [94] K. A. van Riper, *Astrophys. J.* **232** (1979) 558.
- [95] G. Gambino, Ph.D. thesis, University of Palermo (2004).
- [96] W. R. Hix, *et al.*, *Phys. Rev. Lett.* **91** (2003) 201102.
- [97] C. Ishizuka, A. Ohnishi, K. Sumiyoshi, *Nucl. Phys. A* **723** (2003) 517.
- [98] A. S. Botvina, I. N. Mishustin, *Phys. Lett. B* **584** (2004) 233.
- [99] C. J. Horowitz, M. A. Pérez-García, J. Piekarewicz, *Phys. Rev. C* **69** (2004) (4) 045804.
- [100] G. Watanabe, K. Sato, K. Yasuoka, T. Ebisuzaki, *Phys. Rev. C* **69** (2004) (5) 055805 (pages 14).
- [101] E. Baron, J. Cooperstein, S. Kahana, *Phys. Rev. Lett.* **55** (1985) 126.
- [102] M. Takahara, K. Sato, *Astrophys. J.* **335** (1988) 301.
- [103] F. D. Swesty, J. M. Lattimer, E. S. Myra, *Astrophys. J.* **425** (1994) 195.

- [104] K. Sumiyoshi, H. Suzuki, S. Yamada, H. Toki, Nucl. Phys. A **A730** (2004) 227.
- [105] E. Baron, J. Cooperstein, S. Kahana, Nucl. Phys. A **A440** (1985) 744.
- [106] G. M. Fuller, Astrophys. J. **252** (1982) 741.
- [107] J. Cooperstein, J. Wambach, Nucl. Phys. A **420** (1984) 591.
- [108] O. E. B. Messer, Ph.D. thesis, University of Tennessee (2000).
- [109] M. Liebendörfer, O. E. B. Messer, A. Mezzacappa, R. W. Hix, F.-K. Thielemann, K. Langanke, in *Proceedings of the 11th Workshop on “Nuclear Astrophysics”*, edited by W. Hillebrandt, E. Müller (Ringberg Castle, Tegernsee, Germany, 2002), pp. 126–131.
- [110] O. E. B. Messer, M. Liebendörfer, W. R. Hix, A. Mezzacappa, S. W. Bruenn, in *From Twilight to Highlight: The Physics of Supernovae* (2003), p. 70.
- [111] S. W. Bruenn, W. C. Haxton, Astrophys. J. **376** (1991) 678.
- [112] K. Langanke, G. Martínez-Pinedo, J. M. Sampaio, Phys. Rev. C **64** (2001) 055801.
- [113] W. R. Hix, F.-K. Thielemann, Astrophys. J. **511** (1999) 862.
- [114] H. Shen, H. Toki, K. Oyamatsu, K. Sumiyoshi, Nucl. Phys. A **637** (1998) 435.
- [115] H. Shen, H. Toki, K. Oyamatsu, K. Sumiyoshi, Prog. Theor. Phys. **100** (1998) 1013.
- [116] W. R. Hix, A. Mezzacappa, O. E. B. Messer, S. W. Bruenn, J. Phys. G: Nucl. Part. Phys. **29** (2003) 2523.
- [117] M. Liebendörfer, O. E. B. Messer, A. Mezzacappa, W. R. Hix, in *Proceedings of the 20th Texas Symposium on Relativistic Astrophysics*, edited by J. C. Wheeler, H. Martel (AIP, Melville, 2001), pp. 472–477.
- [118] W. R. Hix, Ph.D. thesis, Harvard University (1995).
- [119] A. Mezzacappa, S. W. Bruenn, Astrophys. J. **405** (1993) 637.
- [120] K. Langanke, E. Kolbe, D. J. Dean, Phys. Rev. C **63** (2001) 032801.
- [121] S. E. Koonin, D. J. Dean, K. Langanke, Phys. Repts. **278** (1997) 2.
- [122] J. Pruet, G. M. Fuller, Astrophys. J. Suppl. **149** (2003) 189.
- [123] M. Rampp, H.-T. Janka, private communication.
- [124] W. C. Haxton, Phys. Rev. Lett. **60** (1988) 1999.
- [125] J. M. Sampaio, K. Langanke, G. Martínez-Pinedo, Phys. Lett. B **511** (2001) 11.
- [126] G. M. Fuller, B. S. Meyer, Astrophys. J. **376** (1991) 701.

- [127] J. M. Sampaio, K. Langanke, G. Martínez-Pinedo, D. J. Dean, Phys. Lett. B **529** (2002) 19.
- [128] A. Juodagalvis, K. Langanke, G. Martínez-Pinedo, W. R. Hix, D. J. Dean, J. M. Sampaio, Nucl. Phys. A (2004), in press, [nucl-th/0404078](#).
- [129] K. Langanke, G. Martínez-Pinedo, P. von Neumann-Cosel, A. Richter, Phys. Rev. Lett. (2004), in press, [nucl-th/0402001](#).
- [130] D. Z. Freedman, Phys. Rev. D **9** (1974) 1389.
- [131] D. L. Tubbs, D. N. Schramm, Astrophys. J. **201** (1975) 467.
- [132] S. W. Bruenn, A. Mezzacappa, Phys. Rev. D **56** (1997) 7529.
- [133] N. Itoh, Progress of Theoretical Physics **54** (1975) 1580.
- [134] N. Itoh, H. Totsuji, S. Ichimaru, H. E. Dewitt, Astrophys. J. **234** (1979) 1079.
- [135] C. J. Horowitz, Phys. Rev. D **55** (1997) 4577.
- [136] N. Itoh, H. Hayashi, A. Nishikawa, Y. Kohyama, Astrophys. J. Suppl. **102** (1996) 411.
- [137] R. M. Bionta, G. Blewitt, C. B. Bratton, D. Caspere, A. Ciocio, Phys. Rev. Lett. **58** (1987) 1494.
- [138] K. Hirata, T. Kajita, M. Koshiba, M. Nakahata, Y. Oyama, Phys. Rev. Lett. **58** (1987) 1490.
- [139] E. N. Alekseev, L. N. Alekseeva, I. V. Krivosheina, V. I. Volchenko, Soviet Astronomy Letters **14** (1988) 41.
- [140] J. R. Wilson, in *Relativistic Astrophysics*, edited by J. Centrella, J. LeBlanc, R. Bowers (Jones and Bartlett, 1985), p. 422.
- [141] S. W. Bruenn, T. Dineva, Astrophys. J. **458** (1996) L71.
- [142] A. Burrows, R. Walder, C. D. Ott, E. Livne, in *The fate of the most massive stars* (ASP Conf. Series, 2004), [astro-ph/0409035](#).
- [143] A. Mezzacappa, in *Supernovae as cosmological lighthouses* (2004), [astro-ph/0410085](#).